












# Interferometric Imaging of $\lambda$ Andromedae: Evidence of Starspots and Rotation

J. R. Parks<sup>1</sup>, R. J. White<sup>1</sup> , F. Baron<sup>1</sup> , J. D. Monnier<sup>2</sup> , B. Kloppenborg<sup>1</sup> , G. W. Henry<sup>3</sup> , G. Schaefer<sup>1,4</sup> , X. Che<sup>2</sup>, E. Pedretti<sup>5</sup>, N. Thureau<sup>5</sup>, M. Zhao<sup>6</sup> , T. ten Brummelaar<sup>4</sup> , H. McAlister<sup>4</sup>, S. T. Ridgway<sup>7</sup> , N. Turner<sup>4</sup>, J. Sturmman<sup>4</sup>, and L. Sturmman<sup>4</sup>

<sup>1</sup> Georgia State University, Department of Physics and Astronomy, 25 Park Place South, Suite 605, Atlanta, GA 30303-2911, USA

<sup>2</sup> University of Michigan, Astronomy Department, 1805 S. University Avenue, Ann Arbor, MI 48109-1090, USA

<sup>3</sup> Tennessee State University, Center of Excellence in Information Systems, 3500 John A. Merritt Boulevard, Box No. 9501, Nashville, TN 37203-3401, USA

<sup>4</sup> The CHARA Array, Georgia State University, P.O. Box 3965, Atlanta, GA 30302-3965, USA

<sup>5</sup> University of St. Andrews, Department of Physics and Astronomy, UK

<sup>6</sup> Penn State University, Department of Astronomy and Astrophysics, 401 Davey Lab, University Park, PA 16802, USA

<sup>7</sup> National Optical Astronomy Observatory, NOAO, Tucson, AZ, USA

Received 2019 January 16; revised 2020 August 31; accepted 2020 August 31; published 2021 May 24

## Abstract

Presented are the first interferometric images of cool starspots on the chromospherically active giant  $\lambda$  Andromedae. Using the Michigan Infra-Red Combiner coupled to the Center for High Angular Resolution Astronomy Array, 26 interferometric observations were made between 2008 August 17 and 2011 September 24. The photometric time series acquired at Fairborn Observatory spanning 2008 September 20 to 2011 January 20 is also presented. The angular diameter and power-law limb-darkening coefficient of this star are  $2.759 \pm 0.050$  mas and  $0.229 \pm 0.111$ , respectively. Starspot properties are obtained from both modeled and SQUEEZE reconstructed images. The images from 2010 through 2011 show anywhere from one to four starspots. The cadence in the data for the 2010 and 2011 data sets is sufficient to measure a stellar rotation period based on apparent starspot motion. This leads to estimates of the rotation period ( $P_{2010} = 61 \pm 4.0$  days,  $P_{2011} = 54.0 \pm 2.4$  days) that are consistent with the photometrically determined period of 54.8 days. In addition, the inclination and position angle of the rotation axis are computed for both the 2010 and 2011 data sets; values ( $\bar{\psi} = 21^\circ.5$ ,  $\bar{i} = 78^\circ.0$ ) for each are nearly identical between the two years.

*Unified Astronomy Thesaurus concepts:* Starspots (1572); Interferometry (808); Photometry (1234); Period determination (1211)

## 1. Introduction

In the decades since starspots were first hypothesized by Kron (1947), starspots have been studied, in detail, on scores of other stars. More recently, space missions such as Kepler have increased this number to potentially tens of thousands (Basri et al. 2011). One thing that is certain is starspots are an ubiquitous phenomenon found on stars ranging in age from pre-main-sequence to evolved giants (Strassmeier 2009, and references therein). A motivation for studying starspots is a better understanding of stellar interiors, particularly the origins of magnetic dynamos. Another motivation is that starspots complicate measurements of fundamental stellar properties (e.g.,  $T_{\text{eff}}$ ,  $L$ ,  $RV$ ). Besides the astrophysical importance, if a spotted star happens to harbor orbiting exoplanets, the increased uncertainties in the stellar properties will translate directly to increased uncertainties in the exoplanet properties (e.g., mass, radius). With the advent of millimagnitude photometry, meter-per-second radial velocity surveys, and direct milliarcsecond radius measurements, starspots as a “second-order” effect can no longer be ignored.

To account for the effects of starspots on particular measurements, the starspots themselves must be properly characterized. The bulk of the current understanding of starspot properties (i.e., size, temperature, number, location) stems from two indirect observational techniques of magnetically active stars: light-curve inversion and Doppler imaging. Both methods suffer from certain assumptions that, if incorrect, can lead to unexpected starspot properties or imaging artifacts such as polar starspots or latitudinal starspot belts (Unruh & Collier Cameron 1997; Berdyugina & Tuominen 1998). The

assumptions include a priori knowledge of the stellar inclination for accurate starspot latitude measurements, precise information on stellar parameters, accurate stellar atmosphere models, and accurate atomic and molecular line lists. While the concern that these are artifacts rather than real features has been largely addressed (Unruh 1996; Rice 2002), a more direct method for imaging starspots would bolster confidence in the present results.

Laying aside the veracity of these techniques, the starspot characteristics these techniques have provided in terms of lifetime, size, effect on stellar luminosity, and location are in many cases contrary to the behavior of sunspots. For instance, large starspots are known to persist from months to years (Berdyugina 2005; Strassmeier 2009). However, typical sunspot lifetimes range from days to weeks. The covering factor, or percentage of the visible surface covered by spots, is far larger for active stars (10%–50%) than for the Sun, where the covering factor never exceeds 0.2% (Cox 2000). In addition, at times where the covering factor is largest, the overall luminosity of active stars decreases substantially ( $\Delta V \leq 0.6$ ), whereas the Sun’s overall luminosity actually increases. Sunspots appear at a latitude of  $\sim 30^\circ$  symmetric about the equator at the beginning of the solar activity cycle. As the cycle progresses, sunspots migrate toward the equator, stopping at a latitude of  $\sim 8^\circ$  (Babcock 1961, and references therein). Starspots have been observed to reside anywhere from low to high latitudes or at the poles (Strassmeier 2009, and references therein).

Direct imaging of starspots is needed in order to confirm this discrepancy and potentially link the behavior of magnetic spots from solar-type stars to more active stars. This direct measure

of starspot properties can be obtained via long-baseline optical/near-infrared interferometry (LBI). By combining the light, akin to Young’s double-slit experiment, from multiple, widely spaced telescopes, submilliarcsecond angular resolutions can be achieved. Since the first near-IR aperture synthesis image of the binary Capella by Baldwin et al. (1996), images of binary stars, rapidly rotating stars, and star+disk systems are becoming more commonplace (Tuthill et al. 2001; Kloppenborg et al. 2010; Che et al. 2011; Baron et al. 2012). Additionally, bright, convection-induced starspots have been imaged on the late-type stars Betelgeuse and VX Sagittarii using LBI (Young et al. 2000; Chiavassa et al. 2010). More recently, similar starspots have also been imaged on the surfaces of both RS Per and T Per (Baron et al. 2014).

In terms of magnetically created sunspots, LBI was successful in imaging the spotted surface of  $\zeta$  Andromedae. Roettenbacher et al. (2016) used a technique to image the surface onto a prolate ellipsoid rather than a series of 2D snapshots. The authors discovered a persistent polar spot between two epochs separated by  $\sim 2$  yr. However, the authors do not detect solar-like “active longitudes” of starspot activity, concluding that a different dynamo mechanism than that which operates in the Sun operates in  $\zeta$  And. Clearly, the surfaces of more active stars need to be imaged to support this conclusion.

A truly remarkable study of  $\sigma$  Geminorum ( $\sigma$  Gem) was undertaken by Roettenbacher et al. (2017).  $\sigma$  Gem is an RS CVn system with a spatially resolved primary known to have a spotted photosphere. The authors were able to obtain contemporaneous photometric, spectroscopic, and interferometric data of  $\sigma$  Gem with the intent of comparing and contrasting the three starspot imaging techniques: light-curve inversion, Doppler imaging, and interferometric imaging. Overall, the authors find good agreement between the images produced via each method. Limitations were observed to exist for each method, including but not limited to the following. Light-curve inversion (LCI) cannot confidently constrain starspot latitudes and cannot reproduce complicated starspot configurations. While Doppler imaging improves on producing more complex surface features, the image fidelity is limited by the data quality. Roettenbacher et al. (2017) find that interferometric imaging is the best method for producing images of spotted stellar surfaces. One possible issue with this last method is its inability to reproduce the temperature gradients seen in the Doppler image. However, these gradients may be artifacts in the Doppler image resulting from poor model atmosphere fitting or insufficient rotational phase coverage.

This study intends to add to the collection of directly imaged stellar surfaces with known starspot activity. The observations and data reduction of the target star  $\lambda$  Andromedae are discussed in Section 2. Section 3 describes the methods employed to create both modeled and reconstructed images of the stellar surface. Section 4 discusses the characteristics of the bulk stellar properties provided by these images along with the starspot properties from both the 2010 and 2011 data sets. Additionally, this section compares observed  $V$ -band light curves to synthetic light curves generated from the modeled stellar surfaces. The overall results are summarized in Section 5.

## 2. Observations and Data Reduction

### 2.1. The Chromospherically Active Giant $\lambda$ Andromedae

$\lambda$  Andromedae ( $\lambda$  And; HD 222107) is a bright ( $V$ : 3.872 mag,  $H$ : 1.501 mag) G8 IV–III classified as an RS CVn

type variable star in the Third Catalog of Chromospherically Active Binaries (Eker et al. 2008). Calder (1935) first discovered the photometric variability of  $\lambda$  And with a historical peak  $\Delta V$  amplitude of  $\sim 0.3$  mag. Henry et al. (1995) conducted a 15 yr photometric monitoring campaign and found a periodic variability of  $53.95 \pm 0.72$  days over an  $11.1 \pm 0.4$  yr stellar activity cycle.  $\lambda$  And was found by Walker (1944) to be a single spectroscopic binary with an orbital period of 20.5212 days. Mass estimates for  $\lambda$  And in Donati et al. (1995, hereafter D95) range from 0.65 to  $0.85 M_{\odot}$ , and with considerable uncertainty. From the mass function provided by the spectroscopic orbit, D95 infer a mass ratio  $q = 0.12^{+0.07}_{-0.04}$ . This in turn yields a companion mass of  $0.08\text{--}0.10 M_{\odot}$ , leading to the conclusion that the companion is a low-main-sequence dwarf or high-mass brown dwarf. The high flux contrast between the two components of  $\lambda$  And preclude the companion affecting the photometric or interferometric observations. Nordgren et al. (1999) measured a limb-darkened angular diameter for  $\lambda$  And of  $2.66 \pm 0.08$  mas using the Naval Prototype Optical interferometer in the optical; the measurements spanned 10 spectral channels ranging from 649 to 849 nm. This angular diameter is a factor of  $\sim 5\times$  larger than the  $H$ -band angular resolution provided by the CHARA interferometer. In short,  $\lambda$  And is an interferometrically single, large, bright star with significant variability strongly believed to arise from cool starspots.

Doppler imaging of  $\lambda$  And has not been possible because a low projected rotational velocity ( $v \sin(i) = 6.5 \text{ km s}^{-1}$ ) insufficiently broadens the absorption lines necessary to detect the deformations caused by starspots (Strassmeier 2009). On the other hand, light-curve inversion has been modestly successful in studying starspots on  $\lambda$  And. Frasca et al. (2008, hereafter F08) created a surface map via light-curve inversion of optical photometry coupled with spectral line ratios. This map shows two starspots, each covering  $\sim 8\%$  of the visible surface with temperatures  $\sim 880$  K cooler than the photosphere, separated by  $81^{\circ}$  in longitude. In addition, each starspot is preceded by a bright active region that is comparable in size to the starspot.

### 2.2. Interferometric Observations

For those unfamiliar with the terms and physics behind optical/near-infrared interferometry, an excellent review was written by Monnier (2003).

$\lambda$  And was observed on 26 nights between 2008 August 17 and 2011 September 24. Table 1 lists the dates of the observations, the baselines utilized, the number of [u, v] points, and the calibrators (defined below) used on each night. The parenthetical number beside a calibrator indicates the number of times it was observed during the night. Table 2 contains the uniform disk angular diameters with the error for each calibrator. All observations were conducted using the Center for High Angular Resolution Astronomy (CHARA) array owned and operated by Georgia State University. The array is composed of six 1 m telescopes in a nonredundant Y-shaped configuration. The baseline lengths range from 34 to 331 m, currently making this the longest-baseline optical/near-infrared interferometer in the world (ten Brummelaar et al. 2005); the longest baselines provide an angular resolution of  $\sim 0.4$  mas in the  $H$ -band. The data were collected using the image-plane Michigan Infra-Red Combiner (MIRC) in the  $H$ -band; (see Monnier et al. 2004, 2006 for details). A low-resolution ( $R \sim 42$ ) prism splits the light into eight spectral channels with an absolute

**Table 1**  
CHARA Observing Log

Date <sup>a</sup>	Baselines	Number of [u, v] Points	Calibrators <sup>b</sup>
2008			
Aug 17 (54695.5)	S1-E1-W1-W2	96	37 And (2), 45 Per (3)
Aug 18 (54696.5)	S1-E1-W1-W2	144	$\gamma$ Lyr, 7 And (2), 37 And, $\zeta$ Per (2)
Aug 19 (54697.5)	S1-E1-W1-W2	48	7 And, $\zeta$ Per (2)
Aug 20 (54698.5)	S1-E1-W1-W2	96	7 And (2), 37 And (2), 45 Per (3)
Aug 21 (54699.5)	S1-E1-W1-W2	96	7 And (2), 37 And (2), $\zeta$ Per, 45 Per
Sep 20 (54729.5)	S1-E1-W1-W2	72	7 And (2), $\zeta$ Cas, $\delta$ Per (2)
Sep 27 (54736.5)	S1-E1-W1-W2	72	$\sigma$ Cyg, 37 And (2), $\zeta$ Per (2), tet Gem (3)
2009			
Aug 24 (55067.5)	S1-E1-W1-W2	272	7 And (3), 37 And (2)
	S2-E2-W1-W2		
Aug 25 (55068.5)	S1-E1-W1-W2	432	7 And (4), 37 And (2), HR 75
	S2-E2-W1-W2		
2010			
Aug 2 (55410.5)	S1-E1-W1-W2	168	7 And (2), 37 And
	S2-E2-W1-W2		
Aug 3 (55411.5)	S1-E1-W1-W2	456	$\sigma$ Cyg, 7 And (3), 37 And (2)
	S2-E2-W1-W2		
Aug 10 (55418.5)	S1-E1-W1-W2	432	$\sigma$ Cyg, 7 And (3), 37 And (4)
	S2-E2-W1-W2		
Aug 11 (55419.5)	S1-E1-W1-W2	288	$\sigma$ Cyg, 7 And (4), 37 And (2)
	S2-E2-W1-W2		
Aug 18 (55426.5)	S1-E1-W1-W2	432	$\sigma$ Cyg, 7 And (3), 37 And (5)
	S2-E2-W1-W2		
Aug 19 (55427.5)	S1-E1-W1-W2	432	$\sigma$ Cyg (2), 7 And (5), 37 And (7)
	S2-E2-W1-W2		
Aug 24 (55432.5)	S1-E1-W1-W2	528	$\sigma$ Cyg (2), 7 And (6), 37 And (6)
	S2-E2-W1-W2		
Aug 25 (55433.5)	S1-E1-W1-W2	384	$\sigma$ Cyg (2), 7 And (5), 37 And (2)
	S2-E2-W1-W2		
Sep 2 (55441.5)	S1-E1-W1-W2	528	7 And (7), 37 And (6)
	S2-E2-W1-W2		
Sep 3 (55442.5)	S1-E1-W1-W2	600	7 And (9), 37 And (3)
	S2-E2-W1-W2		
Sep 10 (55449.5)	S1-E1-W1-W2	336	7 And (6), 37 And (2)
	S2-E2-W1-W2		
2011			
Sep 2 (55806.5)	S1-S2-E1-E2-W1-W2	360	$\sigma$ Cyg, 7 And (2), 22 And (3), HR 653
Sep 6 (55810.5)	S1-S2-E1-E2-W1-W2	392	$\sigma$ Cyg, 7 And (2), 22 And (3), HR 653
Sep 10 (55814.5)	S1-S2-E1-E2-W1-W2	360	7 And (2), 22 And
Sep 14 (55818.5)	S1-S2-E1-E2-W1-W2	864	7 And (4), 22 And
Sep 19 (55823.5)	S1-S2-E1-E2-W1-W2	808	7 And (3), 22 And, HR 653 (2)
Sep 24 (55828.5)	S1-S2-E1-E2-W1-W2	200	7 And, 22 And, HR 653 (2), $\eta$ Aur

**Notes.**

<sup>a</sup> The number in parentheses is the approximate MJD.

<sup>b</sup> The number in parentheses is the number of observations during the night.

wavelength precision of  $\pm 0.25\%$  based on measurements of  $\iota$  Peg using the orbit of Konacki et al. (2010).

Interferometric data are collected when the light path difference between each telescope pair is well below the coherence length. This is achieved by “delaying” the light from one telescope by adding more path length to the light of the other telescope through the use of delay lines. When the light paths are equal, the light from each telescope combines as an interference fringe. The MIRC combiner is then set to track these fringes while the data frames are taken. Afterward, a series of calibration frames are recorded that include background and foreground frames, along with images of the light from each beam individually. Collection of the data and

calibration frames typically does not exceed 30 minutes. The total amount of data taken on a particular night is identical to the number of [u, v] points listed in Table 1.

The standard MIRC pipeline was used for data reduction (Monnier et al. 2007). The frames containing the fringe pattern in each block of data were coadded. These coadded frames are corrected for instrumental effects through a background-frame subtraction and foreground-frame normalization. Raw squared visibilities, triple amplitudes, and closure phases are extracted using the Fourier transform of these corrected, coadded frames. Photometric calibration due to differences in the flux amplitude per telescope beam is performed via real-time flux estimates derived from choppers that temporally encode the light from

**Table 2**  
Calibrator Angular Diameters

Calibrator	$\theta_{UD}$ (mas)	References
37 And	$0.682 \pm 0.03$	Kervella & Fouqué (2008)
45 Per	$0.41 \pm 0.02$	Barnes et al. (1978)
$\gamma$ Lyr	$0.676 \pm 0.047$	SearchCal (Bonneau et al. 2006)
7 And	$0.676 \pm 0.047$	SearchCal (Bonneau et al. 2006)
$\zeta$ Per	$0.67 \pm 0.03$	getCal <sup>a</sup>
$\zeta$ Cas	$0.290 \pm 0.020$	SearchCal (Bonneau et al. 2006)
$\delta$ Per	$0.555 \pm 0.038$	SearchCal (Bonneau et al. 2006)
$\sigma$ Cyg	$0.54 \pm 0.02$	Barnes et al. (1978)
tet Gem	$0.813 \pm 0.056$	SearchCal (Bonneau et al. 2006)
HR 75	$1.04 \pm 0.012$	CHARM2 (Richichi et al. 2005)
22 And	$0.591 \pm 0.041$	SearchCal (Bonneau et al. 2006)
HR 653	$0.646 \pm 0.045$	SearchCal (Bonneau et al. 2006)
$\eta$ Aur	$0.336 \pm 0.023$	SearchCal (Bonneau et al. 2006)

**Note.**

<sup>a</sup> <https://nexsci.caltech.edu/software/getCal/>

each telescope (prior to 2010) or through the use of a beam splitter following spatial filtering to shunt part of the beam to a CCD that directly monitors the flux levels from each telescope (Che et al. 2010, after 2010). The data are then transformed from relative measurements to absolute measurements through observations of a calibration star or “calibrator.” A calibrator is a star of known size that is typically on the order of or smaller than the array’s resolution limit and is within a few degrees of the target on the sky.

During 2008 and 2009, only one or two snapshot observations were obtained of  $\lambda$  And. A snapshot observation is where only a single set of data frames bracketed by calibrator observations is taken. While these observations were valuable in confirming the presence of starspots from asymmetric closure phases, the starspots in the resultant images cannot be confirmed as genuine. The discussion of the observational strategy and results of these data sets can be found in the [Appendix](#).

The 2010 observing run combined observations from the S1-E1-W1-W2 and S2-E2-W1-W2 telescope configurations. Each telescope has an alphanumeric designation to describe its location. The letter refers to the baseline direction (“S” for south, “E” for east, “W” for west), while the number indicates the location along that baseline, where “1” is exterior to “2.” The longest CHARA baseline is between E1 and W1. The switch between telescope configurations occurred approximately at the midpoint of the night. In both configurations,  $\lambda$  And was observed continuously with each observation bracketed by an observation of a calibrator. This strategy of telescope configurations, constant monitoring, and bracketed observations is designed to provide well-calibrated measurements sampling the largest [u, v] coverage available. This strategy yields 11 visibilities, eight closure phases, and eight triple amplitudes per spectral channel.

In addition to the above strategy, 2010 data sets consist of observations on sequential nights that were subsequently combined into a single OIFITS file.<sup>8</sup> This strategy provides both an increased [u, v] coverage and a sanity check for the imaging methods because images of the star should be nearly identical between subsequent nights. The only exception to this

<sup>8</sup> OIFITS is the standard file format for optical/near-IR interferometric measurements (Pauls et al. 2005).

strategy is for September 10 and 11, as poor weather prevented observations on the 11th.

The 2011 observing run benefited from the MIRC upgrade that enabled six simultaneous telescope observations. Again to maximize the [u, v] coverage,  $\lambda$  And was observed continuously over the night for as long as the delay lines would permit (typically 6 hr for all six telescopes). Again,  $\lambda$  And measurements were bracketed by measurements of a calibrator star. Each individual observation yields 15 visibilities, 20 closure phases, and 20 triple amplitudes per spectral channel. Since observations from subsequent nights were not combined, the number of [u, v] points obtained is approximately one-half that of the 2010 data set, despite the addition of two telescopes.

### 2.2.1. Interferometric Measurement Errors

Standard errors are propagated for the measured quantities. However, because of systematic effects, two types of error are applied to the calibrated squared visibilities and triple amplitudes to appropriately account for systematics. Additive errors are necessary for two different behaviors in the data. The first is when the calibrated squared visibility or triple amplitude falls below zero. As this is nonphysical, a constant is added to enlarge the error to include zero. The second is when the squared visibilities and triple amplitudes do not monotonically increase or decrease as a function of wavelength across the eight spectral channels. The errors are then enlarged by a multiplicative constant to account for any abnormal structures (e.g., step functions) found in the data across the eight spectral channels. Typical additive errors for the squared visibility and triple amplitude are  $2 \times 10^{-4}$  and  $1 \times 10^{-5}$ , respectively. The multiplicative errors improved after 2010 because of the better photometric calibration provided by the photometric channels. The typical multiplicative errors in squared visibility and triple amplitude are 15% (10%) and 20% (15%), respectively, prior to 2010 (2011).

Typically,  $1^\circ$  is added to the closure phase errors, as suggested by Zhao et al. (2011). In addition, two additional closure phase errors are incorporated to avoid poor model fits due to calibration systematics. These new errors are important in the low signal-to-noise ratio (S/N) regime near visibility null crossings. As correlated camera readout noise dominates the closure phase measurements at low S/N, minimum closure phase errors are applied when the S/N in the triple-amplitude signal is  $\lesssim 1$ . Finite time-averaging and spectral bandpass effects are accounted for by an error term proportional to  $\Delta CP_\lambda$  across each spectral channel;  $CP_\lambda$  corresponds to the closure phase as a function of wavelength. These two errors are applied to the closure phase noise via the equation  $\sigma_{CP} > \text{MAX}((30^\circ / (S/N_{T3amp}^2), 0.2\Delta CP_\lambda))$ , where  $S/N_{T3amp}$  is the S/N in the triple-amplitude measurement.

This study does not account for any errors arising from bandwidth smearing as this is a negligible effect. Given the CHARA array’s operating wavelength ( $H = 1.62 \mu\text{m}$ ) and long baselines, bandwidth smearing will only be a factor on angular sizes of approximately 40 mas or greater. This is far larger than the predicted 2.75 mas for  $\lambda$  And.

### 2.2.2. Identification and Removal of Poor Data

In a few data sets in 2010 and 2011, the visibility in certain blocks of data on certain baseline pairs is not consistent with a simple Bessel function. The reason for these discrepant data

blocks is most likely the poor calibration on that baseline. These discrepancies are found almost exclusively on the short-baseline pairs (e.g., S1–S2, W1–W2, E1–E2). The visibilities were either lower than the visibilities in the other blocks on the same baseline or possessed an opposite or flat slope in comparison to other blocks on the same baseline. The exclusion of these data is unlikely to affect the starspot analysis as these features are unresolved on the shortest baselines. Data was judged to be discrepant via visual inspection and removed prior to either modeling or image reconstruction. At most, the rejected data only amounted to 1% of the total data for any epoch.

### 2.2.3. 37 And

The star 37 And was used as a calibrator, in addition to other calibrators during the same night, for the 2008, 2009, and 2010 observing runs. Che et al. (2012) discovered that 37 And is a high-contrast binary based on sinusoidal-like variations in the closure phase with a few-degree amplitude.

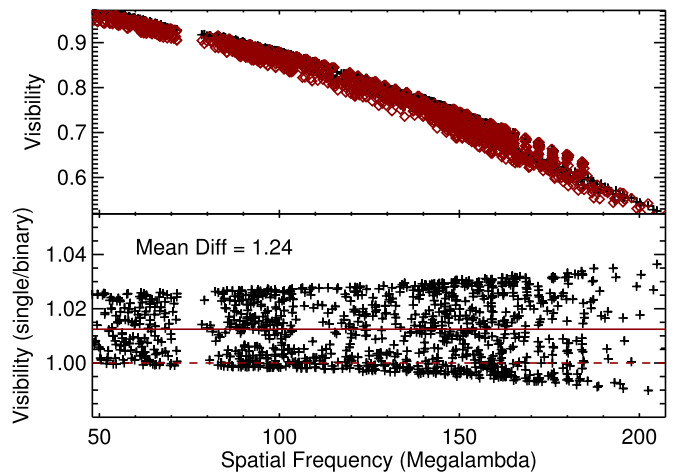
The orbit of the 37 And companion has been fully characterized by R. M. Roettenbacher et al. (2015, in preparation). To study the effect this companion has on  $\lambda$  And data, the visibility and closure phase of a single star (the assumed calibrator) and a binary system (the actual calibrator) are compared to each other. The single star is taken to be a uniform disk with an angular diameter of 0.682 mas. The binary system is composed of the single star and a point source with a flux ratio of 80 (primary/secondary), a semimajor axis of 46.66 mas, and an eccentricity of 0.8405. Given the orbit, the largest component separation was computed to be 82.7 mas, which occurred on September 10. The  $[u, v]$  coverage for this analysis is the same as for September 2 and 3, which represents the densest coverage of any single epoch.

Figure 1 shows both of the visibilities expected from the uniform disk and the binary. Also shown is the uniform disk visibility divided by the binary visibility as a function of baseline. The error introduced increases with baseline to a maximum of 3.6% with an average inflation of 1.24%. Given that the typical multiplicative errors in squared visibilities are 10%–15%, this effect is considered negligible. It should also be noted that this represents the worst contribution made by the binary and does not address the contribution of additional proper calibrators that will mitigate the above effect.

Figure 2 shows the expected zero-closure phase for the single uniform disk. The red diamonds indicate the closure phase signal produced by the binary. The standard deviation of this signal is  $1^\circ.14$ . Given that the noise floor for the  $\lambda$  And measured closure phase is  $1^\circ$ , the effect of the binary is also considered negligible.

## 2.3. Photometric Observations

Photometric observations of  $\lambda$  And were obtained with Tennessee State University’s T3 0.4 m automatic photometric telescope (APT) located at Fairborn Observatory on Mt. Hopkins, Arizona.  $\lambda$  And was observed 376 times over 3.4 yr from 2008 September 20 to 2012 February 1. Figure 3 shows the measured time series. The differential magnitudes were corrected for atmospheric extinction and transformed into the Johnson  $V$  filter system.  $\Psi$  And ( $V$ : 4.982) and  $\kappa$  And ( $V$ : 4.137) were used as the comparison and check star, respectively. The typical photometric error is 6.0 millimag.



**Figure 1.** Top: shown here are both of the visibilities expected from a uniform disk (0.682 mas) and the binary (point source secondary, flux contrast = 80, separation = 82.7 mas). Bottom: this contains the uniform disk visibility divided by the binary visibility as a function of baseline. The solid red line indicates the mean visibility elevation of 1.24%.

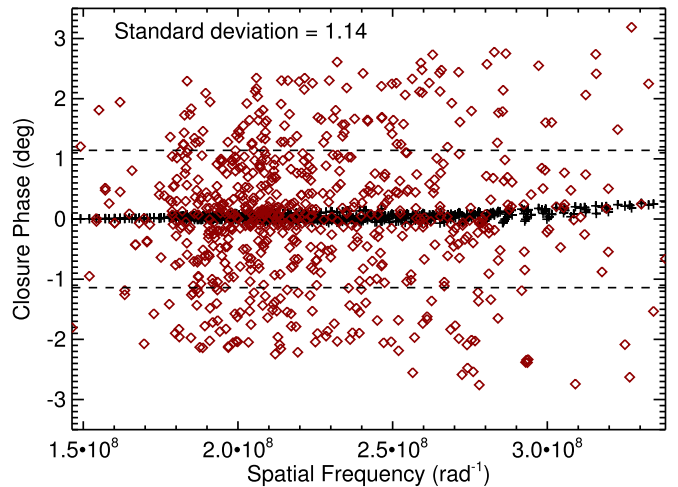


**Figure 2.** Shown here are both of the closure phases expected from a uniform disk and the binary. As expected, the closure phases for the uniform disk are zero, while the standard deviation of the binary closure phases is  $1^\circ.14$ .

These errors are computed from the standard deviations in the time series of the check star.

### 2.3.1. $\lambda$ And Optical Light Curve

The qualitative behavior of the time series (i.e., overall trends, changing variability amplitudes) is consistent with  $\lambda$  And’s 11.1 yr stellar cycle (Henry et al. 1995). The time series can be split into four “seasons”; each season corresponds to photometric observations taken just after the interferometric observations of the same year. The offset between the beginning of the interferometric and photometric observations is about one  $\lambda$  And rotation. The seasons are labeled for the year in which the observations were taken. The time series period and variability amplitude in each season are measured for comparison with the modeled light curves generated from the interferometric images. Table 3 contains the date ranges of each season, along with the identified period and the peak-to-trough  $\Delta V$  amplitude.

**Table 3**  
Photometry Observing Log

Season	Dates (MJD)	$T_0$ (MJD)	$\Delta T$ (days)	$N_{\text{obs}}$	Period (days)	$\Delta V$ (mag)
2008	54729.7979–54861.6223	54722.0	131.8	66	$54.27 \pm 0.032$	0.165
2009	55091.9383–55222.6037	55098.0	130.7	58	$55.15 \pm 0.91$	0.154
2010	55459.7624–55581.6084	55488.7	121.8	73	$53.35 \pm 1.1$	0.099
2011	55823.6466–55958.5967	55813.0	134.9	194	$53.30 \pm 1.9$	0.057

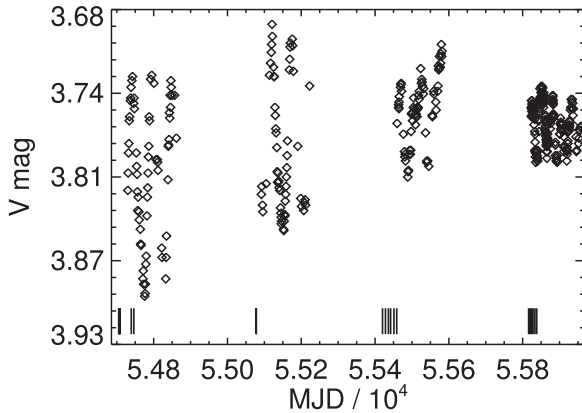


**Figure 3.** Time series photometry for  $\lambda$  And from 2008 September to 2012 February. The tick marks along the bottom axis represent the interferometric observations. The brightening trend of the time series is due to the 11.1 yr stellar cycle (Henry et al. 1995).

The period of photometric variability for the time series in each season is identified using the Plavchan–Parks algorithm (Parks et al. 2014). Figure 4 displays the light curve for each season folded to the most significant period. Uncertainties in the period are set by the width of a Gaussian fit to the most significant peak in the power spectrum. The four periods determined are  $54.27 \pm 0.032$ ,  $55.15 \pm 0.91$ ,  $53.3 \pm 1.1$ , and  $53.3 \pm 1.9$  days. The doubled appearance in season 4 could arise from starspots primarily on longitudes separated by  $\sim 180^\circ$ . In the previous seasons, one or more starspots only dominate a single hemisphere. The average rotation period of  $\lambda$  And is  $54.02 \pm 0.88$  days, where the reported error is the standard deviation of the four measured periods.

### 3. Starspot Analysis

Two different techniques are employed to characterize starspots from the observed interferometric data: a cool, spotted stellar surface model and image reconstruction. These methods are independent of each other; the results of one technique were *not* used as a starting condition for the other.

#### 3.1. Spotted Star Model

The stellar surface model is computed using an IDL code capable of modeling any number of circular cool or hot starspots on a limb-darkened surface. The limb darkening is characterized by a power law as formulated by Hestroffer (1997). The modeled starspots are simplifications intended to identify areas of starspot concentration, from which estimates can be made of stellar rotation and the rotation axis orientation. It is expected that a starspot will not have a regular shape or a constant temperature based on Doppler mapping studies. The free starspot parameters for each starspot are the starspot

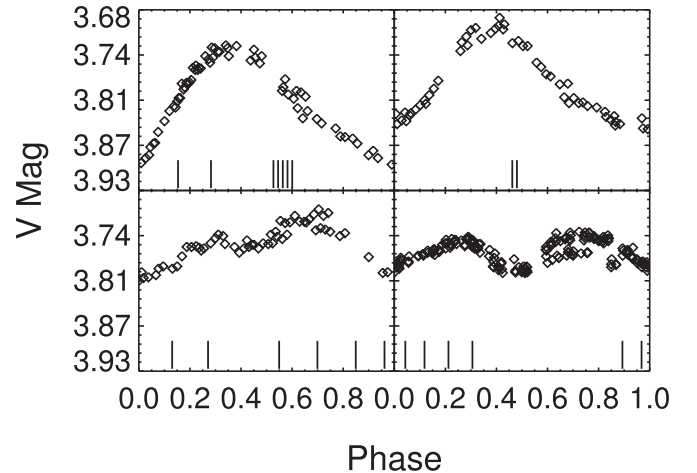


**Figure 4.** Top left: season 2008 time series folded to a period of  $54.27 \pm 0.032$  days. Top right: season 2009 time series folded to a period of  $55.15 \pm 0.91$  days. Bottom left: season 2010 time series folded to a period of  $53.4 \pm 1.1$  days. Bottom right: season 2011 time series folded to a period of  $53.3 \pm 1.9$  days.

covering factor ( $\phi$ ), starspot latitude ( $b$ ), starspot longitude ( $l$ ), and the starspot intensity ratio ( $f$ ). In addition, the code accounts for the effects of foreshortening on starspots located away from the substellar point. The code extracts model interferometric data by computing the Fourier transform of an artificially generated stellar surface projected on the plane of the sky. The sampling for the Fourier transform is taken from the  $[u, v]$  coverage of the observed data being modeled. The goodness-of-fit parameter is the equally weighted reduced  $\chi^2$  average between the observed and modeled visibilities, closure phases, and triple amplitudes.

Changes in the angular diameter and, to a lesser extent, the limb-darkening coefficient have a large effect on modeled visibilities at spatial scales smaller than the first zero of the visibility function. As the starspot information is contained on these smaller spatial scales, accurately determining the stellar properties prior to searching for the starspot properties is needed. This is done by first combining all of the interferometric data from 2010 and 2011 into a single OIFITS file. The  $\theta$  and  $\alpha$  are measured by modeling only the visibility data using a grid search with a parameter step size of  $1 \times 10^{-3}$ . The parameter uncertainty is determined by the lowest reduced  $\chi^2 + 1$  ellipse in the reduced  $\chi^2$  space. The farthest points of the ellipse along each axis are taken as the errors in  $\theta$  and  $\alpha$ , respectively. Figure 5 shows the reduced  $\chi^2$  space for  $\theta$  and  $\alpha$  with the white cross marking the best solution. A slight degeneracy exists between these two parameters, as seen by the elliptically shaped gradients. Closure phases are not considered at this stage;  $\lambda$  And is likely not rotationally ( $v \sin i = 6.5 \text{ km s}^{-1}$ ) or Roche lobe distorted.

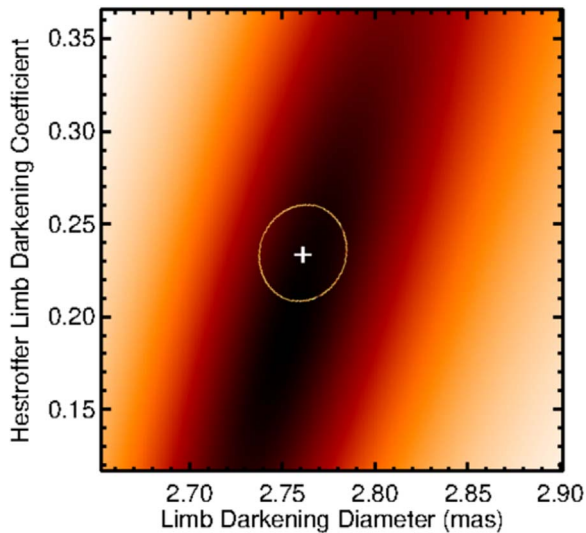


**Figure 5.** The best-fit  $\theta$  and  $\alpha$  are determined through a grid search with a parameter step size of  $1 \times 10^{-3}$ . The reduced  $\chi^2$  space for  $\theta$  and  $\alpha$  is shown with the white cross marking the position of best fit. A slight degeneracy exists between these two parameters, as seen by the elliptically shaped gradients.

Once  $\theta$  and  $\alpha$  are known, model solutions for each epoch are computed using a multiparameter downhill simplex minimization (Press et al. 1992, AMOEBA). As the simplest model that fits the observables is desired, model solutions are generally limited only to one, two, or three starspots. The model with the lowest reduced  $\chi^2$  is chosen as the best surface representation. A fourth starspot model is only investigated if the presence of the additional starspot can be inferred from the prior and subsequent epochs based on rotational grounds. Only cool starspots are modeled as these are the type to persist on the timescale of a stellar rotation. Early attempts with the AMOEBA algorithm on starspot models demonstrated that the solutions are biased by initial parameters and search scales. This is indicative of numerous local minima in the reduced  $\chi^2$  space along with the deeper global minimum. The search scale employed is roughly 10% of the physical range for each parameter. For example, the range in allowable intensity ratios is from 0.5 to 1.0, so the search scale is set to 0.05. AMOEBA is only effective at finding an accurate solution if the search occurs near the global minimum. Therefore, a genetic algorithm is employed prior to running AMOEBA in order to find the approximate location of the reduced  $\chi^2$  global minimum.

A genetic algorithm (GA) is an iterative process through which a best solution is found by “evolving” an initial set of randomly chosen model solutions (i.e., members; Charbonneau 1995). The fitness, or chance it will be used in the subsequent iteration, of each member is determined based on the member’s reduced  $\chi^2$ . The “survival” process is determined via a roulette-wheel scheme. The wheel is spun a number of times equal to the population size. The probability the wheel will choose a member to survive is proportional to the member’s fitness. Therefore, the next population will, in theory, be composed of model solutions with lower reduced  $\chi^2$  on average. This new population is “evolved” via two different random methods: crossover and mutation. Crossover takes sections of a parameter value and swaps it with another parameter value. For example, solution A has a latitude of  $45^\circ 12$ , and solution B has a longitude of  $12^\circ 57$ . Crossover can swap the digits after the decimal to yield a new latitude of  $45^\circ 57$  and longitude of  $12^\circ 12$ . Mutation causes a section of the

parameter value to change randomly. Using the previous example, the latitude  $42^\circ 12$  could mutate to become  $49^\circ 12$ . Both crossover and mutation are applied with a frequency of 90% and 1%, respectively. The fitness of the new population is determined, and the entire process is iterated until the average fitness drops below a convergence criterion.

The AMOEBA algorithm is run to find an accurate solution for the starspot parameters as GA alone does not converge to the minima in reduced  $\chi^2$  space. These starspot parameters are listed in Tables 5 and 8. During the determination of starspot parameters using both the GA and AMOEBA algorithms, the stellar angular diameter and limb-darkening coefficient are kept fixed.

Since the observations occur in the Rayleigh–Jeans tail of the spectral energy distribution, the temperature ratio between a starspot and the photosphere should be a linear function of the corresponding intensity ratio. Therefore, the intensity ratio is directly translated into the starspot temperature ratio,  $T_R$ .

### 3.2. SQUEEZE: Image Reconstruction

Model-based imaging is a very effective tool in determining starspot properties; however, it is limited by the assumptions used to create the model (e.g., circular starspots). Model-independent imaging, or image reconstruction, on the other hand has the freedom to portray more realistic starspot shapes and sizes. The main hurdle faced by image reconstruction is an ill-posed inverse problem brought on by working in a data-starved regime, incomplete [u, v] coverage, and atmosphere-corrupted Fourier phase information. Image-reconstruction algorithms are all based on a regularized maximum-likelihood paradigm that reconciles a  $\chi^2$  statistic with  $k$  number of regularization statistics, or regularizer ( $R_k$ ), modulated by a user-defined weighting parameter ( $\mu_k$ ):

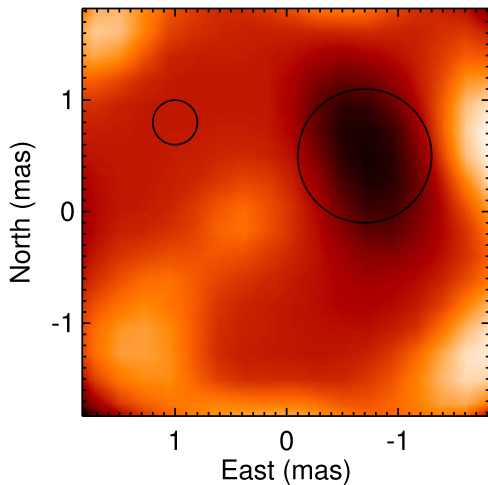
$$\hat{i} = \operatorname{argmax}_{i \in \mathbb{R}^n} \left\{ \chi^2(i) + \sum_{k=1}^K \mu_k R_k(i) \right\}. \quad (1)$$

Image reconstructions abide by two restrictions: the flux in a particular pixel must be nonnegative, and the flux of the reconstructed image is normalized to unity.

The image-reconstruction code SQUEEZE<sup>9</sup> is used on the  $\lambda$  And data sets (Baron et al. 2010); this code is an evolved version of the reconstruction program MACIM (Ireland et al. 2006). The SQUEEZE initial state is a  $50 \times 50$  pixel array of a  $2.777$  mas (a first estimate of  $\theta$  for  $\lambda$  And) uniform disk containing 4000 flux elements. After the initial state is set, SQUEEZE uses a multithread approach, with each thread finding the best image by moving flux from pixel to pixel iteratively via a simulated annealing algorithm. The *total variation* regularizer is chosen as it is designed to minimize brightness gradients across the surface (Rudin et al. 1992). This favors a conservative surface image with a few large starspots as opposed to many smaller ones. Experiments with other regularizers such as Laplacian regularization and the  $\ell_0$  sparsity norm were attempted but failed to produce images with a reduced  $\chi^2$  lower than total variation alone. This is consistent with the findings of Renard et al. (2011), who found total variation outperformed four other regularization methods.

A final image reconstruction is the average of 10 images generated by SQUEEZE. The initial conditions in regards to the initial image (uniform disk), choice of regularizer (total

<sup>9</sup> <https://github.com/fabienbaron/squeeze>



**Figure 6.** Closeup of the SQUEEZE reconstruction for the 2011 September 2 data near an apparent starspot. The black circle on the right shows the aperture used to extract starspot properties from the reconstructed image. The black circle on the left shows the aperture over the “quiet” photosphere. The “quiet” photosphere is defined as a part of the stellar surface devoid of flux gradients. The size of the aperture is identical to the minimum achievable angular resolution.

variation), and hyperparameter are identical for each of the images. The random seed used for the Markov chains to create the image is unique for each image. Prior to being averaged, the 10 images were registered using SPLASH<sup>10</sup> to account for any changes in the image photocenter. The averaging of 10 images attempts to minimize the effect of artifacts potentially caused by the reconstruction process. Starspot parameters are extracted by fitting a circular aperture over identified starspots. This process is illustrated in Figure 6. The aperture size provides the covering factor, and the location of the aperture center provides the starspot latitude and longitude. As the starspot edge is difficult to quantify and the starspot may be irregular in shape,  $\phi$  is only an approximate measure. The intensity ratio is calculated by dividing the flux at the aperture center with a flux measurement of the “quiet” photosphere. The quiet photosphere is identified as a part of the stellar surface devoid of flux gradients. The circular aperture is fit to the reconstructed starspots by eye.

In addition to the creation of a final averaged reconstructed image, an image representing the standard deviation of the 10 iterations is created. The detection strength,  $\sigma_{ds}$ , of the starspot is computed using this mean standard deviation. A circular aperture is placed on the quiet photosphere with a size equal to the minimum angular resolution. The detection strength is the mean flux within this aperture subtracted from the mean flux within the starspot aperture and then divided by the standard deviation.

### 3.2.1. Image Artifacts

A large problem facing image reconstruction is the believability of surface features. Certain results from imaging can be easily dismissed as artifacts, such as hexagonal stellar surfaces or a repeating symmetric pattern of bright spots that is inconsistent with a rotating surface. Certain results can be accepted as believable, such as dark starspots common between the reconstructed and modeled images, because of the

independence between the two imaging methods. However, since single bright starspots were not modeled, this test is unavailable. Therefore, a method must be devised to determine if any imaged bright starspots are real (e.g., flares, plages) or a consequence of the data sampling or image-reconstruction process.

The method used in this analysis is to create synthetic reconstructed images based on the model images. This is done by extracting visibilities, triple amplitudes, and closure phases from each model image with identical data sampling and S/N as the measured data using the OIFITS-SIM tools.<sup>11</sup> The same reconstruction procedure described in Section 3.2 is used to create synthetic reconstructed images from these data. Artifacts due to miscalibrated observables will be features seen in the reconstructed image, but they are absent in both the simulated and model images. Artifacts due to the  $[u, v]$  coverage and the reconstruction process will be features seen in both the reconstructed and simulated images, but not in the true image.

## 4. Discussion

### 4.1. $\lambda$ Andromedae Stellar Properties

The angular diameter and limb-darkening coefficient are determined via the modeling described in Section 3.1. The initial value of  $\theta$  for the AMOEBA code is set to 2.75 mas as determined from the  $\lambda$  And ( $V-K_s$ ) color (van Belle 1999). An initial  $\alpha$  is found by matching a power-law fit to a four-parameter fit from Claret & Bloemen (2011) given the coefficients for a star with  $T_{\text{eff}} = 4750$  K and  $\log(g) = 3.0$  dex (cgs). This yielded a result of  $\alpha = 0.22$ , consistent with results from other power-law fits to interferometric data of late-type giants (Wittkowski et al. 2002, 2006). The search scales were roughly 10% of the initial values. The final results are  $\theta = 2.759 \pm 0.050$  mas and  $\alpha = 0.229 \pm 0.111$ . At a Hipparcos trigonometric distance of  $37.87 \pm 0.21$  mas (van Leeuwen 2007), this angular diameter corresponds to a linear radius of  $7.831^{+0.067}_{-0.065} R_{\odot}$ .

### 4.2. $\lambda$ Andromedae Starspot Properties: 2010 Data Set

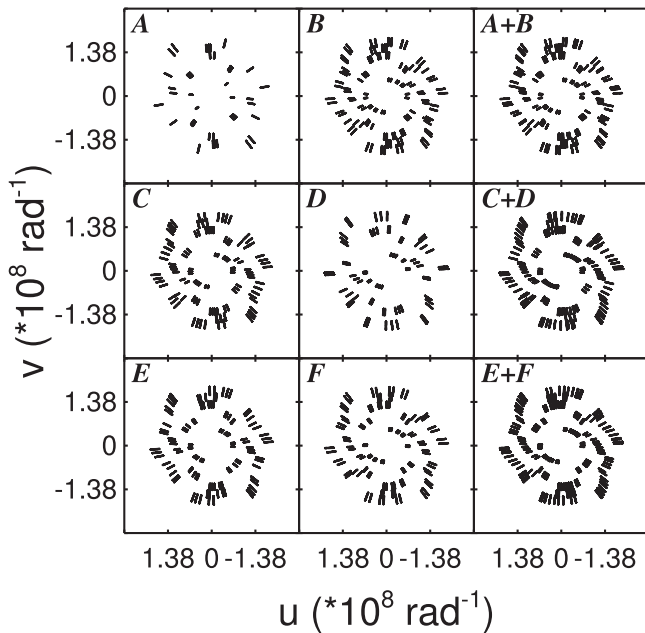
Between 2010 August 2 and September 11, six epochs of data were obtained via the strategy described in Section 2.2. The number of  $[u, v]$  points obtained for each of the five epochs of two combined nights ranged from 624 to 1128, with the densest coverage obtained by the combination of September 2 and 3 (see Table 1). The number of  $[u, v]$  points for the single-night epoch on September 10 is 336. Figures 7 and 8 show the distribution of  $[u, v]$  coverage obtained for each pair of observations. The six epochs are spaced with a cadence between six and nine days corresponding to 10.9%–16.4% of the measured rotation period; significant apparent starspot motion is expected between epochs. The complete observing run spans 71% of one complete  $\lambda$  And rotation period.

Figure 9 shows a distinct nonzero closure phase signature across most sampled spatial scales, pointing to the existence of surface asymmetries. This signature is present in all six epochs. The measured closure phase distribution differs between epochs. Based on the photometric variability and previous starspot imaging of RS CVn stars (Strassmeier 2009, and references therein), the leading hypothesis is that the change in closure phase is due to rotation rather than starspot evolution. In addition, an unspotted model image does not fit the

<sup>10</sup> <https://github.com/fabienbaron/splash>

<sup>11</sup> <https://github.com/bkloppenborg/oifits-sim>





**Figure 7.** The  $[u, v]$  coverage obtained for the first three epochs in 2010. A, August 2; B, August 3; C, August 10; D, August 11; E, August 18; F, August 19.

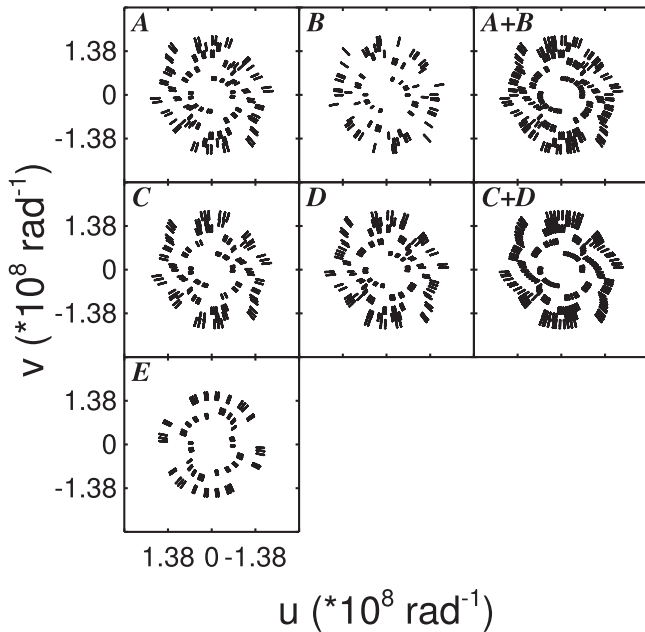


**Figure 8.** The  $[u, v]$  coverage obtained for the second three epochs in 2010. A, August 24; B, August 25; C, September 2; D, August 25; E, September 10.

interferometric data for each epoch in 2010, with the reduced  $\chi^2$  ranging between 15.4 and 44.0.

The best-fit models for each epoch contain between two and four cool starspots. Figure 10 contains the model and reconstructed and simulated images for each epoch. The model reduced  $\chi^2$  ranges between 2.87 and 5.35, with the best fit occurring for August 10 and 11. As an ensemble, the covering factor for individual starspots,  $\phi$ , ranges from 4.0% to 21.8% with a median value of 7.6%. The temperature ratio,  $T_R$ , ranges from 0.756 to 0.907 with a median value of 0.853. Table 4 contains the reduced  $\chi^2$  values corresponding to models with

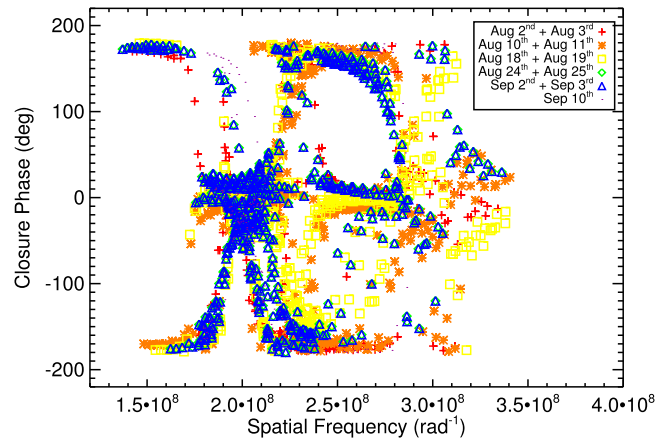


**Figure 9.** Observed closure phases for the 2010 data set. The errors bars, excluded for clarity, range between  $1^{\circ}02$  and  $114^{\circ}$  with a median error of  $3^{\circ}24$ . The distinct nonzero closure phase signature points to surface asymmetries. The differences in the closure phase between nights indicates an evolving asymmetric surface pattern from night to night.

different numbers of starspots. An additional fourth starspot is only included in a model if the reduced  $\chi^2$  improves and the starspot parameters appear consistent with the previous epoch.

The reduced  $\chi^2$  for each reconstructed image is  $\leq 1.01$ . Good qualitative agreement exists between the model and the reconstructed images (see Figure 10). Table 5 contains the measured starspot parameters from both the model and reconstructed images along with the reduced  $\chi^2$  values for the visibility, triple amplitude, and closure phase. This table also contains the difference between the parameters for the same starspot in the model and reconstructed images.

The Epoch 6 model image contains two cool starspots. Although both starspots are listed in Table 5, the starspot located near the northeastern limb ( $b: 55^{\circ}0, l: -40^{\circ}9$ ) is excluded when discussing ensemble starspot properties. The rationale for this decision is that the starspot is nearly twice the size ( $\phi = 44\%$ ) of the next-largest modeled starspot, it is the warmest starspot ( $T_R = 0.925$ ), and it is not reliably seen in the reconstructed image. This “starspot” could be a widely spread patch of starspots, with the covering factor of each individual starspot falling below the resolution limit. The model attempts to reconcile the interferometric signature these starspots produce through the addition of this larger, warmer starspot.

The simulated images and the observing cadence are used to help identify potential artifacts in the reconstructed images. In Epochs 2 through 6, a number of warm starspots are observed in the reconstructed image evenly spaced around the stellar limb. These are rejected as artifacts because of their symmetry and constant position despite the rotating surface. The origin of these artifacts may be the  $[u, v]$  sampling since the pattern of the warm starspots is similar to the pattern of tightly clustered points in the  $[u, v]$  plane (see Figure 8). The southern cool starspot in Epoch 2 is rejected because the covering factor is below the resolution limit. The central warm starspots in the reconstructed images of Epochs 3 and 4 are rejected as artifacts; they are reproduced in the simulated images and are contrary to a rotating surface. The brighter southern pole in Epoch 6 is reproduced in the simulated image and thus rejected. The warm southwestern starspot in Epoch 1, however, cannot be rejected as false as it is not reproduced.

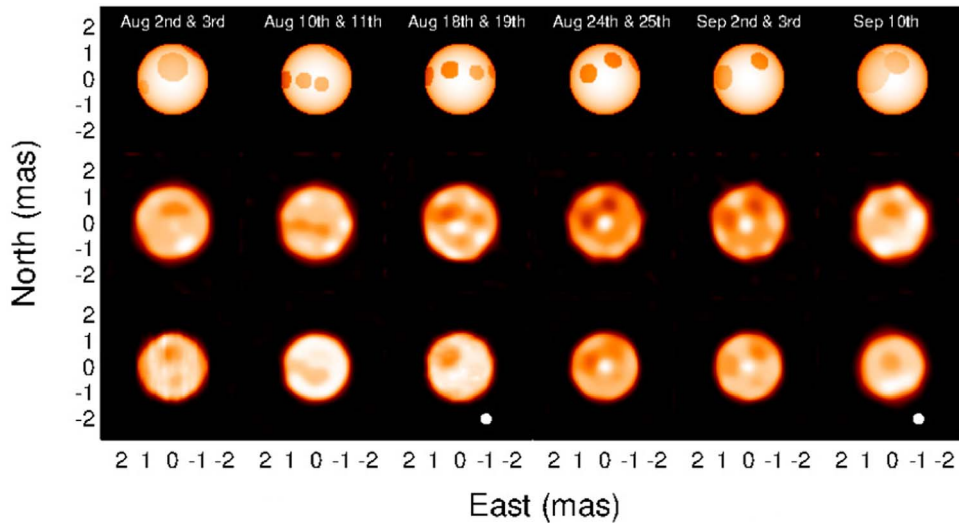


**Figure 10.** Stellar surface images for the 2010 data set. The top row contains the model images, the middle row contains the reconstructed images, and the bottom row contains the simulated images. The white dot in the lower right corner represents the 0.4 mas resolution limit for the CHARA array.

**Table 4**  
Reduced  $\chi^2$  Values for 2010 Model Images

Date	One Starspot	Two Starspots	Three Starspots	Four Starspots
Aug 2 and 3	12.39	6.89	4.92	...
Aug 10 and 11	7.67	5.69	5.00	2.87
Aug 18 and 19	10.35	5.79	4.92	2.88
Aug 24 and 25	10.85	6.97	4.14	...
Sep 2 and 3	8.70	5.35	6.73	...
Sep 10	9.84	4.79	5.30	...

**Note.** Values in boldface are the reduced  $\chi^2$  for the accepted starspot models. A fourth starspot is only added if it improves the fit and is consistent with the preceding and subsequent model images.

#### 4.2.1. Comparison with the 2010 Light Curve

Determining if the starspot imaging provides a picture consistent with the measured photometric time series will provide further confidence in the interferometric results. Season 2010 spans 121.8 days and has a peak-to-trough photometric  $\Delta V$  amplitude of 0.099 mag. The time series begins 10 days after the interferometric observations, providing no simultaneous coverage. The season spans  $\sim 2.2$  rotation periods and varies from one rotation to the next, indicating starspot evolution between rotations. Also, the light curve seems bimodal, suggesting starspots on two active longitudes ( $\phi = 0.3$  and  $0.7$ ). Active longitudes, or longitudes of preferential starspot formation, have been associated with magnetically active stars (Berdyugina 2005). This could be an example of active longitude migration with respect to the star’s rotational frame of reference (Jetsu et al. 1993; Berdyugina & Tuominen 1998; Lanza et al. 1998).

A modeled light curve can be constructed from the best-fit models for each epoch. The change in intensity between an unspotted star and the modeled surface is measured, converted into a  $\Delta$  magnitude, and then scaled for comparison with the observed time series. The scaling is done through an additive constant that shifts the modeled time series to the approximate values of the photometric time series. A multiplicative constant is used to expand the variability amplitude to be comparable to the photometric time series. A modeled light curve is computed and shown in Figure 11 overlaid on top of the photometric time series folded to the 53.35 day period. There is good visible

agreement in all epochs except in Epoch 5, which is brighter than expected. It is difficult to explain the discrepancy based on  $[u, v]$  coverage because this epoch had the densest coverage. Data quality does not seem to be a viable explanation as the errors are not significantly larger than in other epochs and the model reduced  $\chi^2$  is one of the lowest of all six epochs.

#### 4.2.2. Tracing Rotation in the 2010 Data Set

Multiepoch starspot imaging has the potential to trace the stellar rotation via apparent starspot motion. If this motion can be observed, a rotation period can be measured and compared to the period derived from photometry. In addition, the stellar rotation axis can be fully described in both inclination and position angle. Neither Doppler imaging or light-curve inversion has the capacity to determine the latter two quantities. The inclination angle is assumed when using either technique.

The observing baseline for the 2010 data set spans 71% of the photometrically determined rotation period. The cadence will carry starspots  $\sim 47^\circ$  across the stellar surface between epochs assuming a negligible amount of differential rotation.

Individual starspots identified in different epochs are labeled *A* through *G* in Figure 12. Identification of the same starspot in different epochs is judged via visual inspection. Four starspots (*C*, *D*, *E*, *F*) are suspected to exist in three epochs and therefore provide the most useful constraints on the rotation and inclination angle. While the model provides approximate representations of starspots, the changes in  $\phi$  and  $T_R$  are expected to be small as

**Table 5**  
2010 Starspot Properties

MODEL						
Parameter	Epoch 1	Epoch 2	Epoch 3	Epoch 4	Epoch 5	Epoch 6
$\phi_1$ (%)	5.3	7.6	8.4	7.9	13.8	44
$b_1$ (°)	-10.1	0.5	7.1	11.5	4.9	55
$l_1$ (°)	-55.12	-59.4	-64.9	-27.17	-46.8	-40.9
$T_{R1}$	0.926	0.758	0.768	0.772	0.870	0.925
Starspot	C	E	F	F	G	...
$\phi_2$ (%)	20.5	5.8	7.4	7.1	8.0	13.5
$b_2$ (°)	23.5	-1.1	16.4	34.9	31.4	29.84
$l_2$ (°)	3.12	-19.0	-16.4	19.00	24.0	9.7
$T_{R2}$	0.893	0.860	0.758	0.756	0.790	0.898
Starspot	B	D	E	E	F	G
$\phi_3$ (%)	11.5	5.0	5.3	6.3	...	...
$b_3$ (°)	52.5	-6.8	11.0	28.3	...	...
$l_3$ (°)	76.4	10.6	30.4	70.8	...	...
$T_{R3}$	0.801	0.860	0.853	0.853	...	...
Starspot	A	C	D	D	...	...
$\phi_4$ (%)	...	21.8	4.0	...	...	...
$b_4$ (°)	...	54.95	11.8	...	...	...
$l_4$ (°)	...	77.5	68.1	...	...	...
$T_{R4}$	...	0.907	0.853	...	...	...
Starspot	...	B	C	...	...	...
$\chi_{\text{red}}^2$	4.92	2.87	2.88	4.14	5.35	4.79
SQUEEZE						
$\phi_1$ (%)	...	...	...	4.8 (-3.1)	5.8 (-8.0)	...
$b_1$ (°)	...	...	...	3.4 (-8.1)	4.6 (-0.3)	...
$l_1$ (°)	...	...	...	-28.74 (-1.57)	-34.2 (12.6)	...
$T_{R1}$	...	...	...	0.724 (-0.048)	0.817 (-0.053)	...
$\sigma_{\text{ds}}$	...	...	...	11.55	8.35	...
Starspot	...	...	...	F	G	...
$\phi_2$ (%)	9.0 (-11.5)	4.0 (-1.8)	5.76 (-1.64)	4.8 (-2.3)	5.8 (-2.2)	6.8 (-6.7)
$b_2$ (°)	23.6 (-0.1)	-2.3 (-1.2)	16.3 (-0.1)	28.7 (-6.2)	27.4 (-4.0)	21.10 (-8.74)
$l_2$ (°)	2.5 (-0.62)	-27.4 (-8.4)	-22.0 (-5.6)	7.86 (-11.14)	11.7 (-12.3)	0.0 (-9.7)
$T_{R2}$	0.856 (-0.037)	0.856 (-0.004)	0.921 (0.163)	0.724 (-0.032)	0.761 (-0.029)	0.849 (-0.049)
$\sigma_{\text{ds}}$	4.12	7.11	16.20	12.17	9.81	5.46
Starspot	B	D	E	E	F	G
$\phi_3$ (%)	...	4.0 (-1.0)	3.6 (-1.7)	...	...	...
$b_3$ (°)	...	-11.5 (-4.7)	4.6 (-6.4)	...	...	...
$l_3$ (°)	...	9.4 (-1.2)	28.8 (-1.6)	...	...	...
$T_{R3}$	...	0.856 (-0.004)	0.849 (-0.004)	...	...	...
$\sigma_{\text{ds}}$	...	6.28	8.90	...	...	...
Starspot	...	C	D	...	...	...
$\phi_4$ (%)	...	...	2.6 (-1.4)	...	...	...
$b_4$ (°)	...	...	-30.0 (-41.8)	...	...	...
$l_4$ (°)	...	...	2.7 (-65.4)	...	...	...
$T_{R4}$	...	...	0.915 (0.062)	...	...	...
$\sigma_{\text{ds}}$	...	...	6.16	...	...	...
Starspot	...	...	C	...	...	...
$\chi_{\text{red}}^2$	1.00	1.00	1.03	0.98	0.97	0.99

**Note.** The parameters  $\phi_n$ ,  $b_n$ ,  $l_n$ , and  $T_{Rn}$  correspond to the following: the covering factor, the starspot latitude, the starspot longitude, and the fractional temperature with respect to the photosphere. The parenthetical number beside the SQUEEZE parameter values is the difference between the SQUEEZE and model values for the same starspot in each image. For the  $\phi_2$  and  $T_R$  values, a positive number indicates a larger value for the SQUEEZE parameter. For  $b$  and  $l$ , a positive number indicates that the starspot in the SQUEEZE image is farther north and west, respectively.

starspot characteristics only evolve slightly during one stellar rotation. This conclusion is supported by the small changes in  $\phi$  and  $T_R$  reported in Table 6, although the strength of this support is

undercut by a lack of parameter uncertainties. The rotation period based on the motion of modeled starspots ranges from 44.3 to 78.7 days with an average period of  $61 \pm 4.0$  days; the error is the

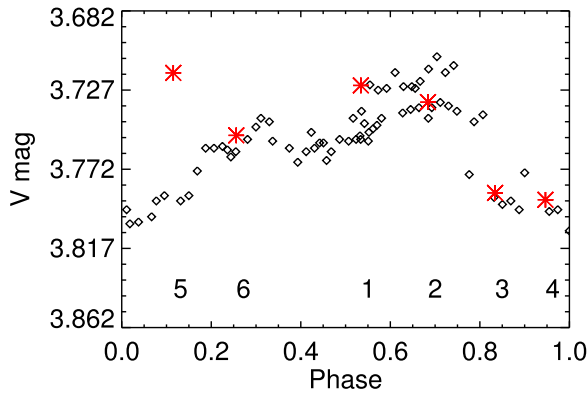


**Figure 11.** Plot of the phased light curve of the V-band photometry for season 2010. The gray diamonds correspond to the V-band time series phased to a period of  $53.3 \pm 1.9$  days. The red asterisks represent the photometry taken from the best-fit models for the six epochs. The numbers along the bottom axis indicate the phase.

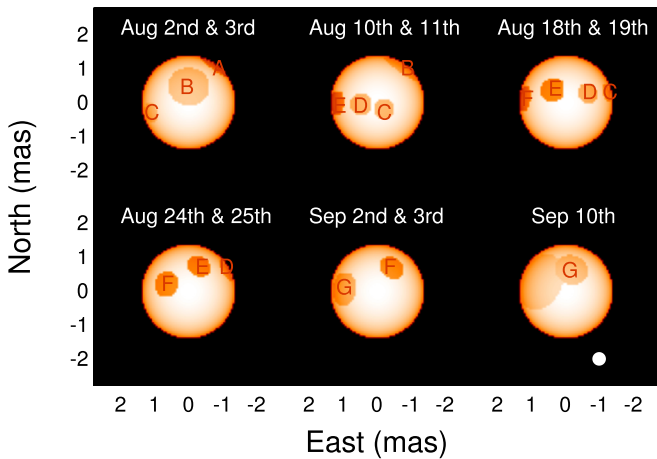


**Figure 12.** Best-fit models for each epoch in 2010. In each model, the starspots are labeled (A through G) to indicate the same starspot as seen in each rotational phase.

standard deviation of the mean. The starspot-determined period is longer than the photometric-determined period of  $54.02 \pm 0.88$  days. This difference is attributed to the low number of times (three) individual starspots are seen to traverse the rotating stellar surface.

Figure 13 shows each of the starspots plotted by longitude versus latitude overlaid by ellipse fits. Estimations of the inclination and position angle of the rotation angle can be made by measuring these elliptical paths. A starspot being carried across the stellar surface via rotation will appear to travel along an elliptical path when viewed in two dimensions. The position angle,  $\Psi$ , is simply the tilt of this ellipse counterclockwise from north (up). The inclination angle,  $i$ , is the inverse sine of the ellipse eccentricity. If the star is viewed face-on, then the starspot will appear to traverse a circular path. Conversely, if the star is viewed edge-on, the starspot will appear to traverse a line. An ellipse is fit via visual inspection to starspots C through F as these spots have been identified in at least three epochs. The average  $\Psi$  and  $i$  are  $19^\circ \pm 8^\circ.1$  and  $75^\circ \pm 5^\circ.0$ , respectively. The errors are the standard deviations of the mean. This inclination angle is higher than the  $60^\circ$  assumed by F08, but is consistent within the uncertainties with the previous inclination estimate  $60_{-15}^{+30}$  by D95. The rotation axis

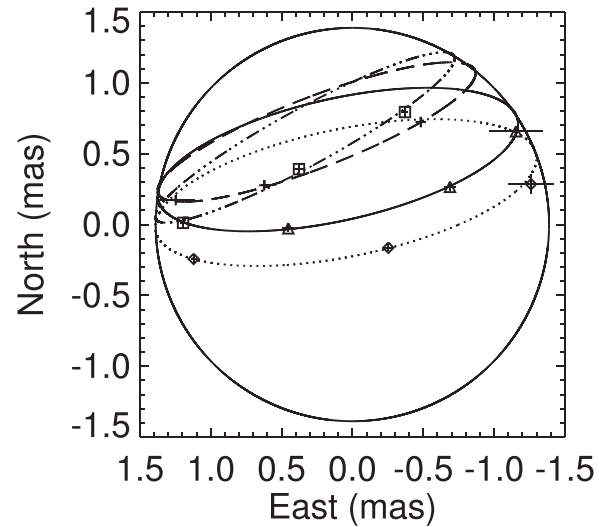


**Figure 13.** Ellipse fits to starspot positions in the 2010 data sets. The dotted line corresponds to spot C. The solid line corresponds to spot D. The dotted-dashed line corresponds to spot E. The dashed line corresponds to spot F. The average computed position angle,  $\Phi$ , and inclination angle,  $i$ , from these fits are  $19^\circ \pm 8^\circ.1$  and  $75^\circ \pm 5^\circ.0$ , respectively. The solid-line circle corresponds to the circumference of  $\lambda$  And.

**Table 6**  
Evidence of Stellar Rotation in the 2010 Data Set

Starspot	Epoch Range	$\Delta\phi$ (%)	$\Delta T_R$	$P_{\text{rot}}$ (days)
B	1 $\rightarrow$ 2	1	-0.014	46.6
C	1 $\rightarrow$ 2	-0.3	-0.066	44.3
	2 $\rightarrow$ 3	-1	-0.007	47.9
D	2 $\rightarrow$ 3	-0.5	-0.007	56.9
	3 $\rightarrow$ 4	1	0.000	70.1
E	2 $\rightarrow$ 3	-0.2	0.000	63.7
	3 $\rightarrow$ 4	-0.3	-0.002	78.7
F	3 $\rightarrow$ 4	-0.5	0.014	77.0
	4 $\rightarrow$ 5	0.1	0.018	63.4
G	5 $\rightarrow$ 6	0	0.028	49.1

is measured to be coming out of the plane of the sky in the northern hemisphere.

#### 4.3. $\lambda$ Andromedae Starspot Properties: 2011 Data Set

Between 2011 September 2 and 24, six epochs of data were obtained for  $\lambda$  And using all six telescopes simultaneously. In order to maximize the [u, v] coverage, observations were taken for as long as delay lines were available. Only one night of data was acquired per epoch, as opposed to the combined nights in 2010. Table 1 contains the number of [u, v] points obtained per observation. The number of [u, v] points achieved ranges from 200 to 864, with the densest coverage obtained on September 14 (see Figure 14). The observing cadence was four or five days corresponding to 7.3% and 9.2% of the rotation period, respectively; all six observations span 40.4% of one rotation period.

Figure 15 shows a distinct nonzero closure phase signature across most sampled spatial scales in all six epochs, pointing to

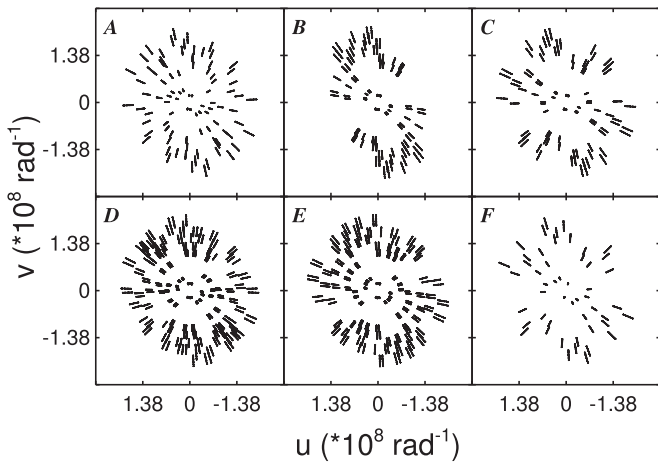


**Figure 14.** The  $[u, v]$  coverage obtained for the 2011 observing run. A, September 2; B, September 6; C, September 10; D, September 14; E, September 19; F, September 24.

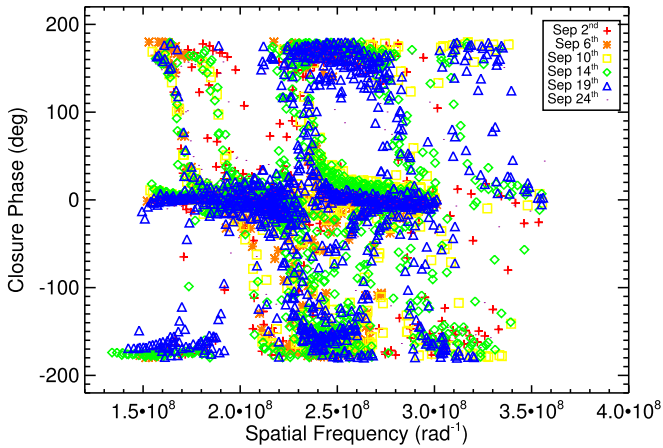


**Figure 15.** Observed closure phases for the 2011 data set. The error bars, excluded for clarity, range between  $1^{\circ}02$  and  $132^{\circ}$  with a median error of  $4^{\circ}62$ . The distinct nonzero closure phase signature points to surface asymmetries. The differences in the closure phase between nights indicate an evolving asymmetric surface pattern from night to night.

an evolving configuration of surface asymmetries. In addition, an unspotted model image does not fit the interferometric data for each epoch in 2011, with the reduced  $\chi^2$  ranging between 9.3 and 16.7.

The best-fit models for each epoch contain one or two cool starspots. The model reduced  $\chi^2$  ranges between 2.91 and 6.24 for these epochs, with the best fit occurring for September 2. Table 7 contains the reduced  $\chi^2$  values corresponding to models with different numbers of starspots. The starspot properties along with the reduced  $\chi^2$  values for visibility, triple amplitude, and closure phase are listed in Table 8. Figure 16 contains the model and reconstructed and simulated images for each epoch. As an ensemble, the covering factor,  $\phi$ , ranges from 10.0% to 16.9% with a median value of 12.5%. The temperature ratio,  $T_R$ , ranges from 0.797 to 0.867 with a median value of 0.849.

The reduced  $\chi^2$  for each of the reconstructed images is at or below 1.02. Good qualitative agreement exists between the model and reconstructed images, but some exceptions do exist (see Figure 16). It is unclear why the western starspot seen in model images is not recovered in the reconstructed images for September 6 and 10. Nor is it clear why there is poor agreement

**Table 7**  
Reduced  $\chi^2$  Values for 2011 Model Images

Date	One Starspot	Two Starspots	Three Starspots
Sep 2	5.72	2.91	6.24
Sep 6	6.24	3.29	7.56
Sep 10	6.01	3.81	5.87
Sep 14	4.13	5.31	...
Sep 19	7.51	6.24	8.29
Sep 24	7.14	5.69	6.16

**Note.** Values in boldface are the reduced  $\chi^2$  for the accepted starspot models.

between the September 19 model and the reconstructed images. In general, the agreement between starspot properties is not as good as it is in the 2010 data set. The reconstructed covering factor is always smaller than the modeled covering factor in each epoch; however, this is not surprising as this parameter should be considered a lower bound. In a trend opposite to 2010, the reconstructed  $b$  is farther north, where it deviates from the model image. No trend exists for when the agreement in  $l$  exceeds the uncertainties.

The reconstructed images in Epochs 1, 3, and 5 contain a ring of warm starspots around the stellar limb. These starspots are rejected as artifacts caused by  $[u, v]$  sampling because of their symmetry and constant location between epochs, which are contrary to starspots on a rotating surface. The following starspots are rejected as artifacts because of the presence of similar features in the simulated image. In Epochs 2 and 4, the warm starspots in the northeast and southwest are rejected as artifacts. The warm northeast starspot in Epoch 3, the warm central starspot in Epoch 4, and the cool southern starspot in Epoch 5 are all rejected as artifacts. The noncircular stellar disk in Epoch 6 is most certainly an artifact, due to the limited number of  $[u, v]$  points (200). In addition, the shape of this disk resembles the configuration of  $[u, v]$  points (see Figure 14).

#### 4.3.1. Comparison with the 2011 Light Curve

Again the measured photometric time series is compared to the imaging results to provide further confidence in the interferometric results. Season 2011 spans 134.9 days and has a peak-to-trough  $\Delta V$  magnitude of 0.057 mag. This season spans  $\sim 2.5$  rotation periods and overlaps the first two epochs of interferometric observations. The folded light curve is double-peaked; this is potentially due to two active longitudes separated by  $\sim 180^{\circ}$ .

A modeled light curve is computed and shown in Figure 17 overlaid on top of the photometric time series folded to the 53.30 day period. The modeled photometry in each epoch is given by the red asterisks and is in agreement with the observed photometry in Epochs 2, 3, and 5. The agreement for Epoch 1 is not as convincing, but not completely inconsistent. However, the modeled photometry for Epochs 4 and 6 visibly disagrees with the observed photometry. The filled blue circles represent the modeled photometry if the parameters for a single starspot are changed. The altered starspots are  $B$  in Epochs 1 and 4 and  $C$  in Epoch 6. The starspot covering factor in both Epochs 1 and 4 is lowered to 11.8%, which is identical to that of Epoch 3, where the starspot is most centrally located. Additionally, the Epoch 4 starspot  $T_R$  is lowered to that of starspot  $B$  in Epoch 3 (0.797). The starspot covering factor in Epoch 6 is lowered to 10.4%, which is the same as the  $\phi$  for the same starspot in Epoch 5.

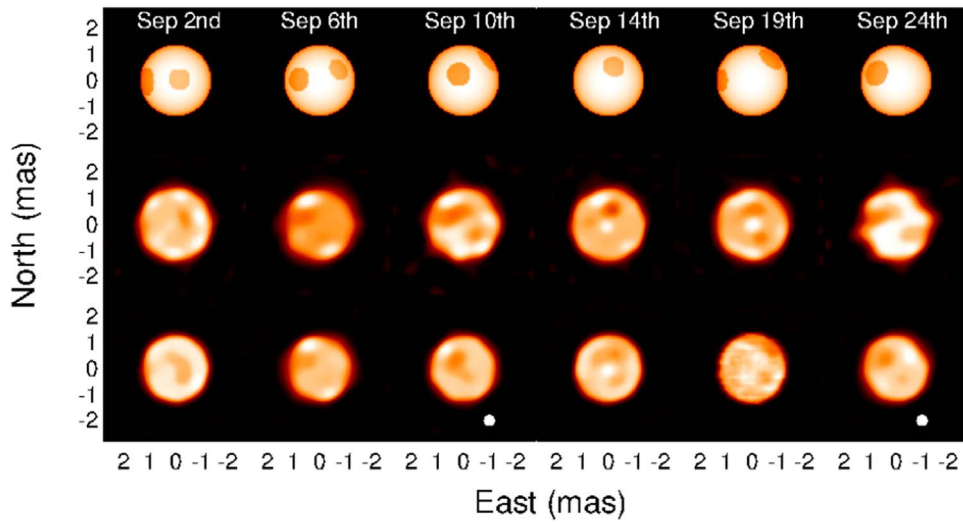


**Figure 16.** Stellar surface images for the 2011 data set. The top row contains the model images, the middle row contains the reconstructed images, and the bottom row contains the simulated images. The white dot in the lower right corner represents the 0.4 mas resolution limit for the CHARA array.

**Table 8**  
2011 Starspot Properties

MODEL						
Parameter	Epoch 1	Epoch 2	Epoch 3	Epoch 4	Epoch 5	Epoch 6
$\phi_1$ (%)	16.9	12.5	11.8	10.2	10.4	14.5
$b_1$ (°)	-1.3	4.15	11.9	24.9	1.30	14.6
$l_1$ (°)	-60.3	-35.6	-7.4	11.8	-60.7	-34.1
$T_{R1}$	0.825	0.825	0.797	0.860	0.825	0.825
Starspot	<i>B</i>	<i>B</i>	<i>B</i>	<i>B</i>	<i>C</i>	<i>C</i>
$\phi_2$ (%)	10.0	10.0	14.7	...	14.8	15.6
$b_2$ (°)	3.65	20.1	37.7	...	40.5	62.1
$l_2$ (°)	8.58	38.1	68.1	...	49.8	85.6
$T_{R2}$	0.864	0.864	0.867	...	0.842	0.849
Starspot	<i>A</i>	<i>A</i>	<i>A</i>	...	<i>B</i>	<i>B</i>
$\chi_{\text{red}}^2$	2.91	3.29	3.81	4.13	6.24	5.69
SQUEEZE						
$\phi_1$ (%)	...	4.0 (-8.5)	7.8 (-4.0)	4.8 (-5.4)	4.0 (-6.4)	...
$b_1$ (°)	...	11.54 (7.39)	16.3 (4.4)	24.8 (-0.1)	-22.33 (-23.63)	...
$l_1$ (°)	...	-29.3 (6.3)	-14.5 (-7.1)	6.3 (-5.5)	14.4 (75.1)	...
$T_{R1}$	...	0.839 (0.014)	0.751 (-0.046)	0.701 (-0.159)	0.849 (0.024)	...
$\sigma_{\text{ds}}$	...	9.09	5.59	9.67	3.23	...
Starspot	...	<i>B</i>	<i>B</i>	<i>B</i>	<i>C</i>	...
$\phi_2$ (%)	4.8 (-5.2)	...	...	2.6	4.8 (-10.0)	...
$b_2$ (°)	9.21 (5.56)	...	...	3.4	24.8 (-15.7)	...
$l_2$ (°)	12.88 (4.30)	...	...	-31.4	5.1 (-44.7)	...
$T_{R2}$	0.860 (-0.004)	...	...	0.915	0.849 (0.007)	...
$\sigma_{\text{ds}}$	5.31	...	...	3.38	3.18	...
Starspot	<i>A</i>	...	...	<i>B</i>	<i>B</i>	...
$\chi_{\text{red}}^2$	1.01	1.02	0.98	0.99	0.95	0.97

**Note.** The parameters  $\phi_n$ ,  $b_n$ ,  $l_n$ , and  $T_{Rn}$  correspond to the following: the covering factor, the starspot latitude, the starspot longitude, and the fractional temperature with respect to the photosphere. The parenthetical number beside the SQUEEZE parameter values is the difference between the SQUEEZE and model values for the same starspot in each image. For the  $\phi_2$  and  $T_R$  values, a positive number indicates a larger value for the SQUEEZE parameter. For  $b$  and  $l$ , a positive number indicates that the starspot in the SQUEEZE image is farther north and west, respectively.

#### 4.3.2. Tracing Rotation in the 2011 Data Set

The observing baseline for the 2011 data set spans  $\sim 41\%$  of the photometrically determined rotation period. The cadence

will carry starspots  $\sim 7\%$  across the stellar surface between epochs assuming a negligible amount of differential rotation. Figure 18 shows a compelling pattern of stellar rotation by three starspots labeled *A* through *C*. Starspot *B* is seen in all six

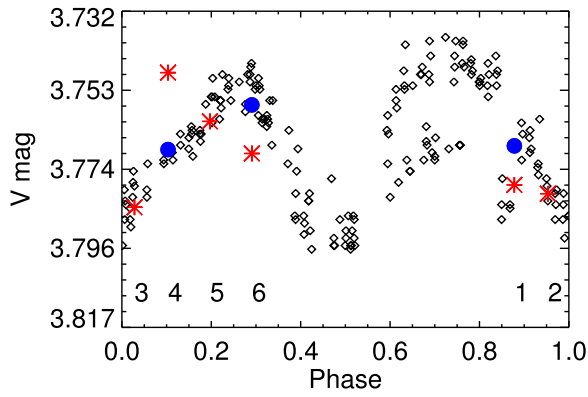


**Figure 17.** Phased light curve of the V-band photometry for Season 2011. The gray diamonds correspond to the V-band time series phased to a period of  $53.3 \pm 1.9$  days. The red asterisks represent the photometry taken from the best-fit models for the six epochs. The filled blue circles represent model photometry where the values of  $\phi$  or  $T_R$  have been altered (see text).

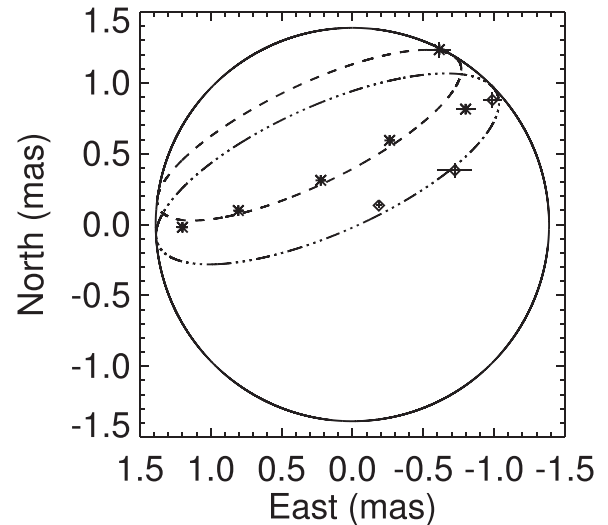


**Figure 19.** Ellipse fits to starspot positions in the 2011 data sets. The dashed line corresponds to the fit to spot A. The dashed-dotted line corresponds to spot B. The average computed position angle,  $\Phi$ , and inclination angle,  $i$ , from these fits are  $24^\circ 9 \pm 1^\circ 2$  and  $66^\circ 4 \pm 4^\circ 4$ , respectively. The solid-line circle corresponds to the circumference of  $\lambda$  And.

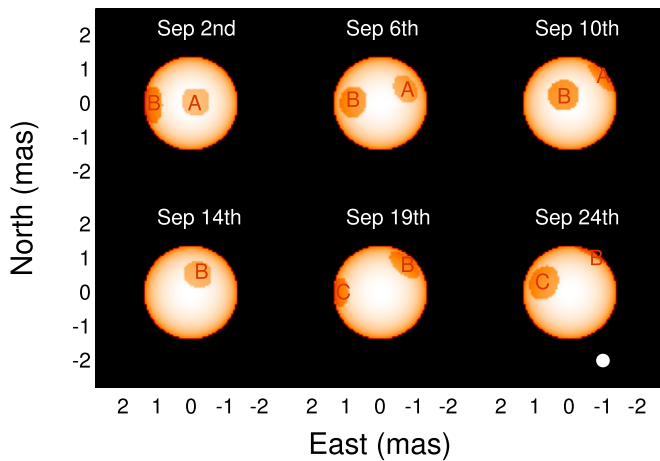


**Figure 18.** Best-fit models for each night in 2011. In each model, the starspot (s) are labeled (A, B, and C) to indicate the same starspot as seen in each rotational phase.

epochs and provides the best estimates of both the stellar rotation and rotation axis. The observing strategy behind the 2011 data set was designed to provide an increased number of measurements for any individual transiting starspot(s). This is done to shrink the uncertainties in the estimates of the rotation axis computed from the 2010 data set. The uncertainties in this estimate are believed to arise from the sparse number of modeled starspots traversing the rotating surface.

Table 9 contains the changes in  $\phi$  and  $T_R$  for starspots A, B, and C and the computed rotation period based on the measured angle between starspot positions from one epoch to the next. The median change in  $\phi$  and  $T_R$  for any starspot over the observed rotation is  $2^\circ 85$  and  $0.050$ , respectively. Considering there is no obvious pattern to these changes coupled with the poor qualitative fit between model and reconstructed images, the changes most likely arise from the approximate nature of the modeling. The range in the measured rotation period based on apparent starspot motion is 43.4 to 64.6 days with an average rotation period of  $54.0 \pm 2.4$  days, which is nearly equal to the photometric rotation period of  $54.02 \pm 0.88$  days. The error is the standard deviation of the mean in the individual rotation periods.

Figure 19 shows each of the starspots plotted by latitude versus longitude overlaid by ellipse fits. For starspots A and B, an ellipse

**Table 9**  
Evidence of Stellar Rotation in the 2011 Data Set

Starspot	Epoch Range	$\Delta\phi$ (%)	$\Delta T_R$	$P_{\text{rot}}$ (days)
A	1 → 2	0	0.000	43.4
	2 → 3	4.7	0.003	45.9
B	1 → 2	-4.9	0.000	56.7
	2 → 3	-0.7	-0.028	49.8
	3 → 4	-1.6	0.063	64.6
	4 → 5	4.6	-0.035	51.1
	5 → 6	0.8	0.007	59.2
C	5 → 6	4.1	0.000	61.2

is fit via visual inspection. The C starspot is excluded from this analysis because it has only two data points. The average  $\Psi$  and  $i$  are  $24^\circ 9 \pm 1^\circ 2$  and  $66^\circ 4 \pm 8^\circ 0$ , respectively. The rotation axis is tilted out of the plane of the sky in the northern hemisphere. These values and orientation are consistent within the errors to the estimates found by the 2010 data sets.

#### 4.4. Comparing Results with Previous Work

Having demonstrated that starspot properties can be measured for  $\lambda$  And using interferometric observations, these results are compared to the results of previous investigations. The approximate nature of starspots in this work allows only for a rough comparison that is intended to highlight general agreement or disagreement with past work.

D95 created a surface map of  $\lambda$  And via a matrix LCI technique using Johnson BV light curves spanning one rotation period. D95 models the observed light curve using two starspots with  $T_R = 0.83 \pm 0.06$ . One starspot is located at  $b = 50^\circ$  with  $\phi = 8\%$ . The other starspot is located at  $b = 20^\circ$  with  $\phi = 4\%$ . The starspots are separated by  $140^\circ$  in longitude. Both the latitudes and covering factors for these starspots are consistent with those identified in this work. However, the temperature ratio in D95 is less than that measured for both the

2010 (median  $T_R = 0.853$ ) and 2011 (median  $T_R = 0.853$ ) data sets.

A more recent study of the starspot properties of  $\lambda$  And was performed by F08. They used a two-component LCI method using Johnson  $V$ -band photometry coupled with spectral line depth ratios to create a map of starspots on  $\lambda$  And. The results of F08 are very consistent with that of D95, with the modeled surface containing two cool starspots each with  $T_R = 0.815_{-0.036}^{+0.064}$ . The covering factors for the two starspots are 8.7% and 3.6% located at latitudes  $57^\circ$  and  $9^\circ$ , respectively. The starspots are separated by  $81^\circ$  in longitude. As with D95, the positions and covering factors of the starspots identified by F08 are consistent with the starspots imaged in this work. However, the temperature ratio is significantly less. One additional difference between F08 and this work, as well as D95, is the modeling of two plage regions by F08. These bright regions are similar in size to the modeled cool starspots. The plages are also in similar locations only offset from the starspots by  $\sim 20^\circ$  in longitude and  $\sim 7^\circ$  in latitude. By design, no hot starspot/plage regions were modeled in this work, but the reconstructed images show no convincing evidence that these exist at any observed epoch.

## 5. Summary

$\lambda$  Andromedae, a bright ( $V$ : 3.872 mag,  $H$ : 1.501 mag) G8 giant, has a long recorded history of consistent sinusoidal-like photometric variability. This variability is believed to result from the rotational modulation of cool starspots. Using light-curve inversion techniques, the presence of starspots has been indirectly revealed (Donati et al. 1995; Frasca et al. 2008). Long-baseline optical/near-infrared interferometry has the potential to directly detect and measure the characteristics of these starspots. LBI has already directly imaged a number of astrophysical systems (e.g., close binaries, circumstellar disks, rapidly rotating stellar surfaces) with unprecedented angular resolution.

$\lambda$  And was observed using the MIRC beam combiner on the CHARA array for 26 days spanning 2008 August 17 to 2011 September 24. The observing strategy evolved over time with upgrades in the MIRC beam combiner. Contemporaneous photometric observations are also available from 2008 September 20 to 2011 January 20. The photometry provides an independent relative estimate of starspot coverage that can be compared to the imaging results.

The CHARA array observations in 2010 employed an observing strategy designed to maximize the  $[u, v]$  coverage. The images created from the 2010 data feature one to four starspots at each of the six epochs. As an ensemble, the median value in the starspot covering factor is 7.6%. The median value of the temperature ratio between starspot and the surrounding photosphere is 0.853. The observing cadence between the six epochs in 2010 is between six and nine days, corresponding to 10.9% to 16.4% of the rotation period. The observations span 71% of one rotation cycle. By measuring the apparent motion of four starspots for three epochs, the rotation period is measured and the rotation axis is determined. The rotation period based on starspot motion is  $61 \pm 4.0$  days, which is longer than the photometric rotation period of  $54.8 \pm 1.9$  days. The rotation axis is tilted out of the plane of the sky in the north with an inclination of  $75^\circ 0 \pm 5^\circ 0$  and a position angle of  $19^\circ 0 \pm 8^\circ 1$ .

A photometric  $V$ -band time series is available beginning 10 days after the last interferometric observation in 2010. The short-cadence time series spans approximately two rotations of  $\lambda$  And. The flux variability in the modeled time series follows the behavior of the photometric time series quite well when the proper scaling factors are applied, with the exception of a single epoch. The discrepancy in this epoch is difficult to explain based on  $[u, v]$  coverage or data quality.

In 2011,  $\lambda$  And was observed for a single night on six different nights using six telescopes simultaneously. This strategy substantially increased the number of visibilities and closure phases obtained for each block of data compared to 2010. However, the  $[u, v]$  coverage decreased by appropriately a factor of 2 because the data were only composed of a single night per epoch. Consequently, the model and reconstructed images are not as consistent as those created from the 2010 data. One to two starspots are identified in the model images for each epoch. As an ensemble, the median value of the starspot coverage is 7.6%, and the median temperature ratio is 0.853. The 2011 observing cadence is four or five days, corresponding to 7.3% and 9.2% of the rotation period and spanning  $\sim 40\%$  of one rotation. One starspot is imaged in all six epochs and is used to measure a rotation period of  $54.0 \pm 2.4$  days, which is nearly identical to the photometric rotation period of  $54.8 \pm 1.9$  days. The rotation axis points out of the plane of the sky in the north with an inclination of  $65^\circ 7 \pm 8^\circ 0$  and a position angle of  $24^\circ 1 \pm 6^\circ 8$ . These values are consistent with the orientation computed from the 2010 data set.

The photometric  $V$ -band time series starting in 2011 overlaps the last two interferometric epochs and spans  $\sim 2.5$  rotations of  $\lambda$  And. The flux variability in the modeled time series follows the behavior of the photometric time series only for half of the epochs. The discrepant epochs can be made to agree with the photometry if the covering factor or the temperature ratios are changed for a single starspot. The parameters are changed to be identical to parameters identified for the same starspot in a different epoch where the starspot is more centrally located.

Using the combined 2010 and 2011 data sets, we find that the measured angular diameter of  $\lambda$  And is  $2.759 \pm 0.050$  mas with a power-law limb-darkening coefficient of  $0.229 \pm 0.111$ . At a Hipparcos trigonometric distance of  $37.87 \pm 0.21$  mas, this yields a linear radius of  $7.831_{-0.065}^{+0.067} R_\odot$ . The angular diameter is consistent with that previously found by Nordgren et al. (1999;  $2.66 \pm 0.08$  mas).

The 2010 and 2011 data sets have provided a convincing picture of starspots on the surface of  $\lambda$  And in support of the closure phase information and the variable light curve. There is qualitative consistency between the modeled and reconstructed images for both the 2010 and 2011 data sets. In addition, the starspots produce a flux variability that is consistent with that observed photometrically just subsequent to the interferometric observations. There is evidence to suggest that starspots imaged in one epoch are again imaged in subsequent epochs. This allows for the determination of rotation periods derived from the 2010 and 2011 data sets. While the 2010 period is longer than the photometrically determined period, the 2011 period is nearly identical to the photometric period. This difference in agreement has been attributed to the number of starspots used to trace the rotation. This method, additionally, allows for the complete characterization of the rotation axis of  $\lambda$  And.



It should be noted that this is a pilot study designed to demonstrate the feasibility of interferometrically imaging starspots on  $\lambda$  Andromedae. An upcoming work will use more sophisticated model and image-reconstruction techniques with the aim of measuring the differential rotation of  $\lambda$  And.

The authors will now express our thanks to our anonymous referee for their conversation and comments. We would also like to express our thanks to both Dr. Chris Farrington and P.J. Goldfinger for their smooth operation of the CHARA Array. We wish to acknowledge Rachael Roettenbacher for her considerable help with quantifying the effect 37 And had on our measurements. This work has made use of data from the European Space Agency (ESA) mission Gaia (<https://www.cosmos.esa.int/gaia>), processed by the Gaia Data Processing and Analysis Consortium (DPAC, <https://www.cosmos.esa.int/web/gaia/dpac/consortium>). Funding for the DPAC has been provided by national institutions, in particular the institutions participating in the Gaia Multilateral Agreement. We would like to acknowledge funding from the National Science Foundation grants AST-0707927 and AST-1108963 awarded to the University of Michigan. Additional NSF funding was provided through the AST-1445935 and AST-1009643 grants awarded to Georgia State University. G.W.H. acknowledges long-term support from NASA, NSF, Tennessee State University, and the State of Tennessee through its Centers of Excellence program.

### Appendix Early Imaging Attempts

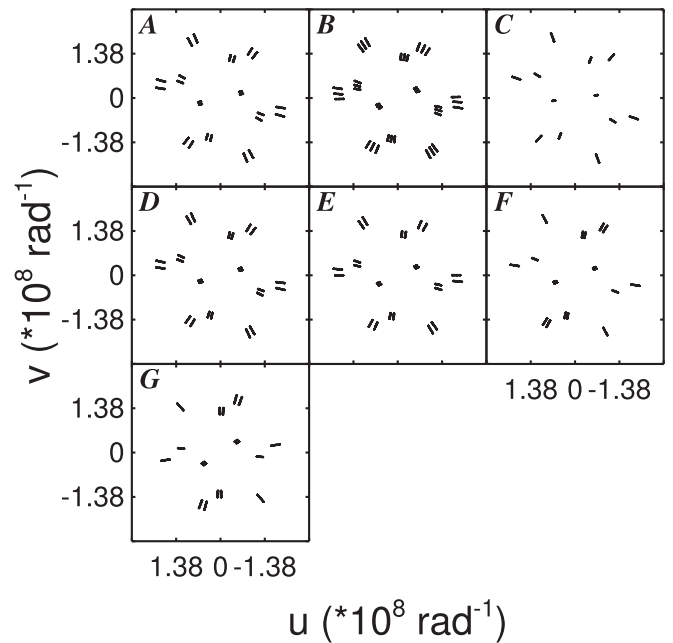
This appendix discusses the failed attempts at high-fidelity surface imaging to illustrate the effect of insufficient  $[u, v]$  coverage on interferometric starspot imaging. Any successful program will need to be designed to maximize this coverage as much as possible. The inconsistent results measured in 2008 are first discussed and then followed by a discussion of the intriguing, yet inconclusive, results measured in 2009.

#### A.1. 2008 Data Set

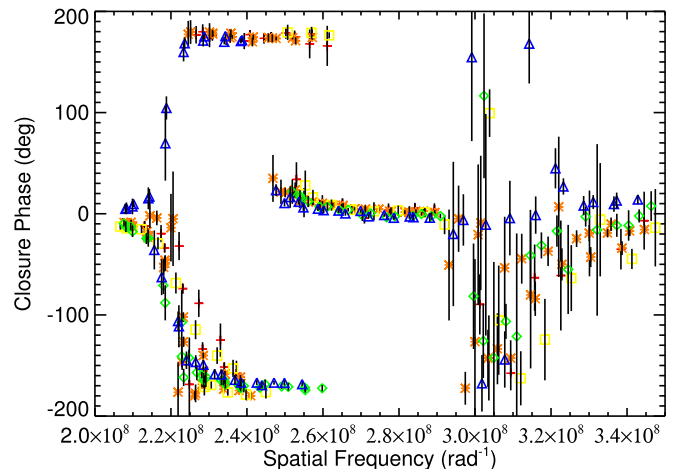
In 2008, two observing runs of  $\lambda$  And were performed, one in August and the other in September. Both runs employed “snapshot” observations using the S1-E1-W1-W2 telescopes. These observations consist of only two or three bracketed observations per night. The August run was composed of observations taken on five consecutive nights between the 17th and the 21st. The  $[u, v]$  coverage achieved ranged from 48 to 144 data points, with the densest coverage obtained on August 18. Figure A1 contains the plots of these  $[u, v]$  configurations. The September run was composed of two observations taken a week apart on the 20th and the 27th. Figure A1 contains the  $[u, v]$  configurations for these nights.

Figure A2 shows a distinct nonzero closure phase signature across most sampled spatial scales for all five days. Unlike in 2010 and 2011, the closure phase signature changes only slightly from night to night, consistent with the hypothesis of surface asymmetries that have not evolved on short timescales. An unspotted model image yields a poor fit to the interferometric data for each epoch, with the reduced  $\chi^2$  ranging between 5.6 to 18.

The reduced  $\chi^2$  values for each modeled epoch in the 2008 August data set are all below 2.85, with the lowest reduced  $\chi^2$  (1.14) occurring on August 19. Despite this, these images do



**Figure A1.** The  $[u, v]$  coverage obtained for the 2008 observing run. A, August 17; 2010: B, August 18; C, August 19; D, August 20; E, August 21; F, September 20; G, September 27.



**Figure A2.** Observed closure phases for the 2008 August data sets. Red cross: August 17. Orange asterisks: August 18. Yellow squares: August 19. Green diamonds: August 20. Blue triangles: August 21. The distinct nonzero closure phase signature points to surface asymmetries. The similarity in the closure phase between nights indicates a consistent asymmetric surface pattern from night to night.

not present a consistent starspot configuration, as can be seen in Figure A3. This figure contains the model, reconstructed, and simulated images for August 17, 18, and 19. The one-day cadence should present nearly identical surface images as the surface only rotates 1.8% from night to night. Starspot evolution on this timescale is not typical for magnetically active stars (Berdyugina 2005; Strassmeier 2009). Additionally, the reconstructed images do not even contain any conclusive evidence for starspots.

The likely factors contributing to the nondetection of a consistent starspot configuration include, but are not limited to, poor  $[u, v]$  sampling and miscalibration.

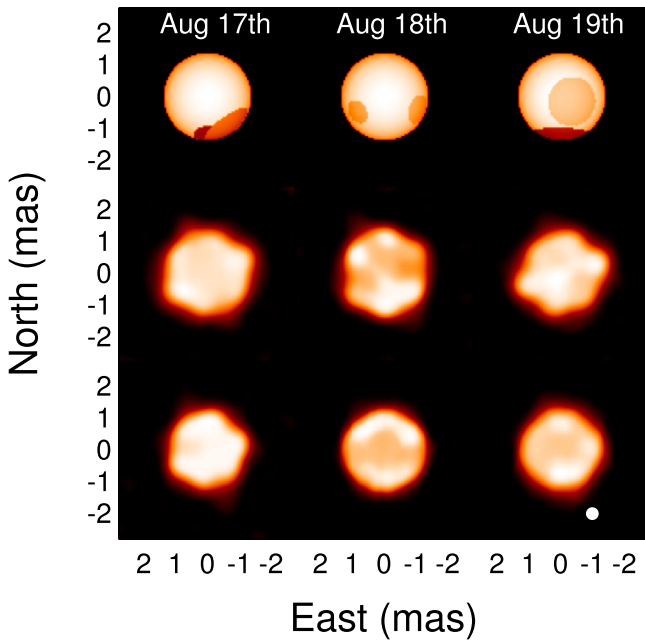


**Figure A3.** Results from the 2008 August 17, 18, and 19 data sets, including the model images (top row), reconstructed images (middle row), and simulated images (bottom row). The white dot in the lower right corner represents the 0.4 mas resolution limit for the CHARA array.

The phased photometric time series (Figure 4) indicates these interferometric observations were taken  $\sim 11$  days after maximum brightness. As shown in the study by Henry et al. (1995), the maximum brightness of  $\lambda$  And can vary by as much as 0.05 mag in the  $V$ -band. This would indicate that even at a time of maximum brightness the visible surface still contains starspots. Therefore, the inconsistent images are probably not due to an insufficient starspot presence.

Thus, despite strong evidence for starspots on the surface of  $\lambda$  And during these epochs, from both measured nonzero closure phases and the variable light curve, the  $[u, v]$  coverage using four telescopes on a single night is insufficient to confidently determine starspot properties.

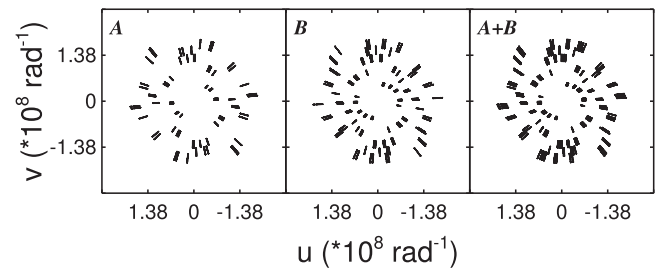
### A.2. 2009 Data Set

The  $\lambda$  And data set in 2009 consists of two observations on August 24 and 25 that are combined to increase the final  $[u, v]$  coverage. Given a rotation period of 55.15 days, starspots will migrate across the surface, as stated above, 1.8% over one night, so the combination of these two nights is not believed to adversely affect the quality of the extracted properties. Each night is the combination of observations using both the S1-E1-W1-W2 and S2-E2-W1-W2 telescope arrays. Figure A4 shows the distribution of the 704  $[u, v]$  points obtained for the merged pair of observations.

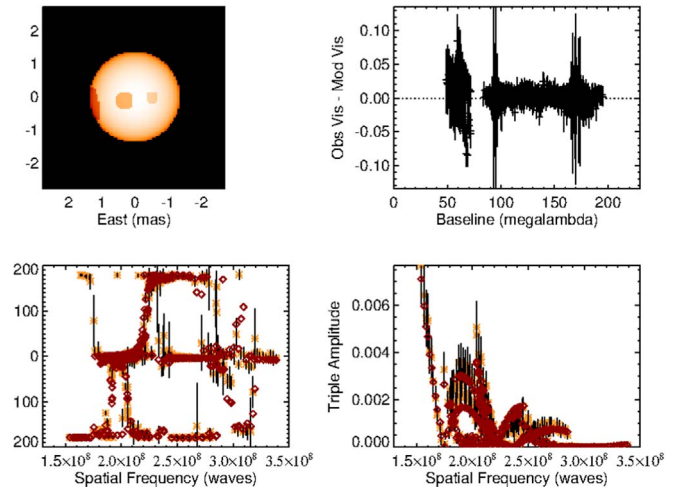
Season 2009 spans 130.7 days or  $\sim 2.4$  rotation periods and has a  $\Delta V = 0.154$  mag. From one rotation to the next, the starspot properties do not appear to change significantly, as illustrated by the low scatter compared to observation errors in Figure 4.

Figure A5 clearly shows nonzero closure phases at both the lower and higher sampled spatial scales. An unspotted model image does not fit well with the measured interferometric data, resulting in a reduced  $\chi^2 = 5.9$ .

The best-fit model (reduced  $\chi^2 = 1.44$ ) contains three cool starspots. Figure A5 contains the best-fit model image along with



**Figure A4.** The  $[u, v]$  coverage obtained for the 2009 data sets. A, August 24; B, August 25.



**Figure A5.** Best-fit results for the 2009 August 24 + August 25 data sets. Top left: model image. Top right: observed minus modeled visibilities as a function of baseline. Bottom left: closure phase as a function of spatial frequency. The orange asterisks indicate observed data, and the red diamonds are the modeled fit. Bottom right: triple amplitudes as a function of spatial frequency. The symbols mean the same as in the closure phase plot.

the model fits to the visibilities, triple amplitudes, and closure phases. The starspot properties are listed in Table A1. Figure A6 contains the final model and reconstructed and simulated images for the 2009 data set. The modeled starspot on the eastern limb was not conclusively detected in the reconstructed image. The properties of the two reconstructed starspots are nearly identical to that of the corresponding modeled starspots, to within errors. The western modeled and reconstructed starspots are included in the final results despite the measured covering factor of both being close to or below the CHARA array’s angular resolution (0.4 mas or  $\phi = 2.1\%$ ). The potential starspots are accepted because the model reduced  $\chi^2$  is worse without its inclusion and the reconstructed starspot  $\sigma_{ds}$  is 3.64.

Two bright starspots are visible on the western limb; each starspot lies nearly equidistant above and below an east–west “equator.” These starspots are not visible in the simulated image. This allows for the possibility that these starspots are genuine surface features.

Based on the phased time series (see Figure 4), the interferometric observations were taken near maximum brightness. However, as discussed in Appendix A.1, it is possible for starspots to be present on the visible surface even at maximum brightness. Given a rotation east to west, the identification of a large, cool starspot on the eastern limb would cause a drop in observed flux, as indicated by the photometry, as it rotates into view.

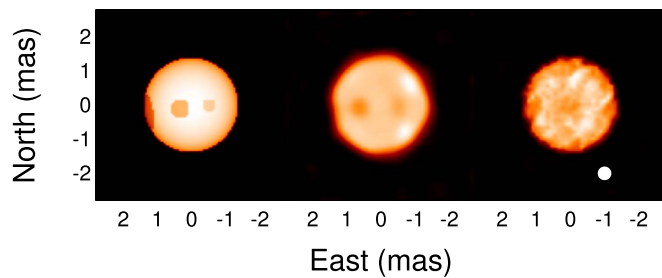


**Figure A6.** Results from the 2009 August 24 + August 25 data set, including the model images (left), reconstructed images (middle), and simulated images (right). The white dot in the lower right corner represents the 0.4 mas resolution limit for the CHARA array.

**Table A1**  
2009 Starspot Properties

Parameter		August 24 + 25	
		Model	SQUEEZE
$\phi_1$	(%)	16.0	...
$b_1$	( $^\circ$ )	-8.6	...
$l_1$	( $^\circ$ )	-76.0	...
$T_{R1}$		0.961	...
$\sigma$		...	...
$\phi_2$	(%)	4.1	3.6
$b_2$	( $^\circ$ )	-2.3	-3.4
$l_2$	( $^\circ$ )	-13.4	-26.8
$T_{R2}$		0.931	0.922
$\sigma$		...	4.8
$\phi_3$	(%)	2.2	2.0
$b_3$	( $^\circ$ )	-0.8	-2.3
$l_3$	( $^\circ$ )	22.9	21.1
$T_{R3}$		0.979	0.924
$\sigma$		...	3.6
Reduced $\chi^2$		1.44	0.93

The observing strategy of combining two consecutive nights of data provides a near 500% gain in the best [u, v] coverage obtained in 2008. This has produced a much improved consistency between the model image and the reconstructed image along with a better quality of fit in both cases. However, the lack of multiple epochs precludes consistency checks or a measure of the rotation period.

#### ORCID iDs

R. J. White <https://orcid.org/0000-0001-5313-7498>  
 F. Baron <https://orcid.org/0000-0002-5074-1128>  
 J. D. Monnier <https://orcid.org/0000-0002-3380-3307>  
 B. Kloppenborg <https://orcid.org/0000-0003-0350-5453>  
 G. W. Henry <https://orcid.org/0000-0003-4155-8513>  
 G. Schaefer <https://orcid.org/0000-0001-5415-9189>  
 M. Zhao <https://orcid.org/0000-0002-4258-9517>  
 T. ten Brummelaar <https://orcid.org/0000-0002-0114-7915>  
 S. T. Ridgway <https://orcid.org/0000-0003-2557-7132>

#### References

- Babcock, H. W. 1961, *ApJ*, **133**, 572  
 Baldwin, J. E., Beckett, M. G., Boysen, R. C., et al. 1996, *A&A*, **306**, L13  
 Barnes, T. G., Evans, D. S., & Moffett, T. J. 1978, *MNRAS*, **183**, 285  
 Baron, F., Monnier, J. D., Kiss, L. L., et al. 2014, *ApJ*, **785**, 46  
 Baron, F., Monnier, J. D., & Kloppenborg, B. 2010, *Proc. SPIE*, **7734**  
 Baron, F., Monnier, J. D., Pedretti, E., et al. 2012, *ApJ*, **752**, 20  
 Basri, G., Walkowicz, L. M., Batalha, N., et al. 2011, *AJ*, **141**, 20  
 Berdyugina, S. V. 2005, *LRSP*, **2**, 8  
 Berdyugina, S. V., & Tuominen, I. 1998, *A&A*, **336**, L25  
 Bonneau, D., Clause, J.-M., Delfosse, X., et al. 2006, *A&A*, **456**, 789  
 Calder, W. A. 1935, *BHarO*, **899**, 13  
 Charbonneau, P. 1995, *ApJS*, **101**, 309  
 Che, X., Monnier, J. D., Kraus, S., et al. 2012, *Proc. SPIE*, **8445** (0)  
 Che, X., Monnier, J. D., & Webster, S. 2010, *Proc. SPIE*, **7734**  
 Che, X., Monnier, J. D., Zhao, M., et al. 2011, *ApJ*, **732**, 68  
 Chiavassa, A., Lacour, S., Millour, F., et al. 2010, *A&A*, **511**, A51  
 Claret, A., & Bloemen, S. 2011, *A&A*, **529**, A75  
 Cox, A. N. 2000, *Allen's Astrophysical Quantities* (New York: AIP)  
 Donati, J.-F., Henry, G. W., & Hall, D. S. 1995, *A&A*, **293**, 107  
 Eker, Z., Ak, N. F., Bilir, S., et al. 2008, *MNRAS*, **389**, 1722  
 Frasca, A., Biazzo, K., Taş, G., Evren, S., & Lanzafame, A. C. 2008, *A&A*, **479**, 557  
 Henry, G. W., Eaton, J. A., Hamer, J., & Hall, D. S. 1995, *ApJS*, **97**, 513  
 Hestroffer, D. 1997, *A&A*, **327**, 199  
 Ireland, M. J., Monnier, J. D., & Thureau, N. 2006, *Proc. SPIE*, **6268**  
 Jetsu, L., Pelt, J., & Tuominen, I. 1993, *A&A*, **278**, 449  
 Kervella, P., & Fouqué, P. 2008, *A&A*, **491**, 855  
 Kloppenborg, B., Stencel, R., Monnier, J. D., et al. 2010, *Natur*, **464**, 870  
 Konacki, M., Muterspaugh, M. W., Kulkarni, S. R., & Helminiak, K. G. 2010, *ApJ*, **719**, 1293  
 Kron, G. E. 1947, *PASP*, **59**, 261  
 Lanza, A. F., Catalano, S., Cutispoto, G., Pagano, I., & Rodono, M. 1998, *A&A*, **332**, 541  
 Monnier, J. D. 2003, *RPPH*, **66**, 789  
 Monnier, J. D., Berger, J.-P., Millan-Gabet, R., & ten Brummelaar, T. A. 2004, *Proc. SPIE*, **5491**, 1370  
 Monnier, J. D., Pedretti, E., Thureau, N., et al. 2006, *Proc. SPIE*, **6268**  
 Monnier, J. D., Zhao, M., Pedretti, E., et al. 2007, *Sci*, **317**, 342  
 Nordgren, T. E., Germain, M. E., Benson, J. A., et al. 1999, *AJ*, **118**, 3032  
 Parks, J. R., Plavchan, P., White, R. J., & Gee, A. H. 2014, *ApJS*, **211**, 3  
 Pauls, T. A., Young, J. S., Cotton, W. D., & Monnier, J. D. 2005, *PASP*, **117**, 1255  
 Press, W. H., Teukolsky, S. A., Vetterling, W. T., & Flannery, B. P. 1992, *Numerical Recipes in C. The Art of Scientific Computing* (Cambridge: Cambridge Univ. Press)  
 Renard, S., Thiébaud, E., & Malbet, F. 2011, *A&A*, **533**, A64  
 Rice, J. B. 2002, *AN*, **323**, 220  
 Richichi, A., Percheron, I., & Khristoforova, M. 2005, *A&A*, **431**, 773  
 Roettenbacher, R. M., Monnier, J. D., Korhonen, H., et al. 2016, *Natur*, **533**, 217  
 Roettenbacher, R. M., Monnier, J. D., Korhonen, H., et al. 2017, *ApJ*, **849**, 120  
 Rudin, L. I., Osher, S., & Fatemi, E. 1992, *PhyD*, **60**, 259  
 Strassmeier, K. G. 2009, *A&ARv*, **17**, 251  
 ten Brummelaar, T. A., McAlister, H. A., Ridgway, S. T., et al. 2005, *ApJ*, **628**, 453  
 Tuthill, P. G., Monnier, J. D., & Danchi, W. C. 2001, *BAAS*, **33**, 861  
 Unruh, Y. C. 1996, in *IAU Symp. 176, Stellar Surface Structure*, ed. K. G. Strassmeier & J. L. Linsky (Dordrecht: Kluwer), 35  
 Unruh, Y. C., & Collier Cameron, A. 1997, *MNRAS*, **290**, L37  
 van Belle, G. T. 1999, *PASP*, **111**, 1515  
 van Leeuwen, F. 2007, *A&A*, **474**, 653  
 Walker, E. C. 1944, *JRASC*, **38**, 249  
 Wittkowski, M., Aufdenberg, J. P., Driebe, T., et al. 2006, *A&A*, **460**, 855  
 Wittkowski, M., Schöller, M., Hubrig, S., Posselt, B., & von der Lühse, O. 2002, *AN*, **323**, 241  
 Young, J. S., Baldwin, J. E., Boysen, R. C., et al. 2000, *MNRAS*, **315**, 635  
 Zhao, M., Monnier, J. D., Che, X., et al. 2011, *PASP*, **123**, 964